Memoirs of the School of Engineering, Nagoya University
Vol.48, No.2 (1996)

DEVELOPMENT AND APPLICATIONS OF NEW POSITION-SENSITIVE RADIATION DETECTORS

Chizuo MORI

Department of Nuclear Engineering

(Received November 15, 1996)

Abstract

The research work in our laboratory since 1982 on the development of position-sensitive nuclear radiation detectors and on their applications is reviewed.

The work started on a simple position-sensitive proportional counter for the precise measurement of radioactivity of gaseous samples without suffering the end effect in a proportional counter, which was successfully adopted in some research institutes.

For neutron measurement, various types of ^{3}He proportional counters were developed; slender counters to be inserted into narrow spaces, nuclear fission counters etc. Detectors which can be inserted into extremely narrow spaces to measure neutron flux distributions were developed using an optical fiber whose tip was coated with a mixture of scintillator, neutron converter and adhesive material. They can be used for the measurement of the distributions of thermal neutrons, fast neutrons or γ-rays by changing the material of the converter. They are being adopted in some research laboratories.

Imaging Plate was newly applied to the measurement of natural radioactivity distributions contained in vegetables, meat and other natural substances. The images are very effective to let the publics realize the presence of natural radioactivity.

Keywords: position-sensitive radiation detector, proportional counter, neutron, optical fiber, imaging plate, radioactivity

Contents

I. Introduction

Position-sensitive radiation detectors have been remarkably developed in a couple of ten years owing to new requirements, and the availabilities of new radiation sources, new materials and new signal processing methods. The development has brought new applications and it is still progressing. In such a spectacular stream of research work, we also concerned ourselves in this field for these 15 years.

Development of position-sensitive radiation detectors with new concepts and new ideas, and their new applications are really interesting work. The followings are some results of our

research work; position-sensitive proportional counters (PSPC) and their applications, optical fiber position detectors and their applications, and Imaging Plate (IP) with their applications.

II. Position-Sensitive Proportional Counters

Position-sensitive proportional counters (PSPC) are divided into multi-wire type and a single wire type in structure and into charge-division method, rise-time method and delay-line method in signal processing.

First we chose a PSPC of a resistive single anode wire type with charge division method for its structural simplicity and appropriateness for the application to internal gas counting which we intended to have the application from the beginning.

2.1 General characteristics

Charge signals Q_L and Q_R in Fig. 2-1 are expressed by the following equations[2-1];

$$Q_L(x, t) = \frac{2Q}{\pi} \sum_{n=1}^{\infty} \frac{1}{n} \sin\left(\frac{n\pi}{l}x\right) \left\{1 - \exp\left(-\frac{n^2\pi^2 t}{rcl^2}\right)\right\} \tag{2-1}$$

$$Q_R(x, t) = -\frac{2Q}{\pi} \sum_{n=1}^{\infty} \frac{1}{n} \cos n\pi \sin\left(\frac{n\pi}{l}x\right) \left\{1 - \exp\left(-\frac{n^2\pi^2 t}{rcl^2}\right)\right\} \tag{2-2}$$

where Q: total induced charge on the anode wire
l: length of the wire
x: radiation incident position

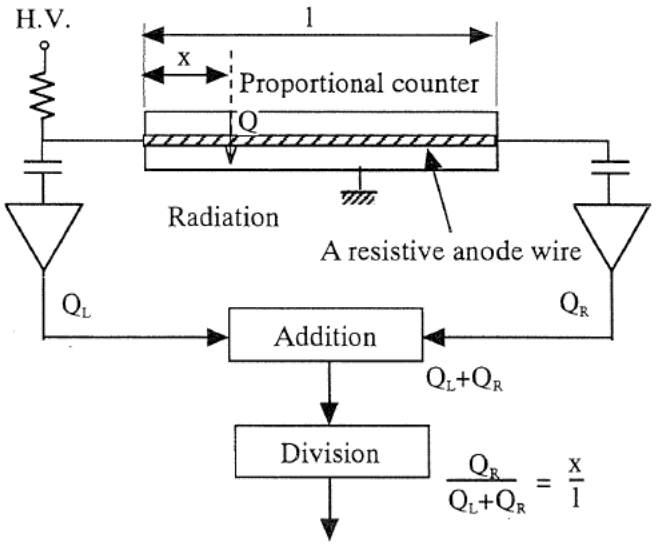

Fig. 2-1 Principle of obtaining a position information.

t: time after the incidence
r: electric resistance per unit length
c: electric capacitance per unit length

When t goes to infinite, $Q_L(x) = Q(1-x)/l$ and, $Q_R(x) = Q\ x/l$ by referring the Fourier series. Then the following equation is obtained

$$Q_R/(Q_L + Q_R) = x/l \tag{2-3}$$

2.2 β, X-ray position-sensitive proportional counter

Our original aim of the development of PSPC was the application to the absolute radioactivity determination of gaseous samples. In the course of the applicative work, we could have some developments with new ideas as follows.

2.2.1 Some new developments

2.2.1.1 Carbon fiber anode wire

Carbon fibers made of acrylic fibers are commercially available inexpensively and have widely been used as structural materials in various fields owing to its high specific strength and modulus. In addition, the distinguished frictional, heat and chemical resistances and electrical properties are finding a wider range of the application of the fiber. The properties of commercially available carbon fibers are confined to 7 μm in diameter, about 300 kg/mm^2 in tensile strength which is several times larger than steel wire's, about 1.8 in density and about 1.5×10^{-3} Ωcm in specific resistance.

A single carbon fiber was stretched[2-2] over a length of 555 mm at an axis of a cylindrical cathode with an inner diameter of 40 mm of a proportional counter. The counter cathode had a narrow and long window along the direction of the cathode axis to permit the incidence of X-rays. A gas mixture of Ar (50%) and CH_4 (50%) was used as a counting gas. Manganese KX-rays, collimated to a width of 0.39 mm, emitted from an ^{55}Fe source were injected through the window. A linear relation between the injected position and the calculated position with Eq. (2-3) was observed. The standard deviation of the relative difference was 0.345%.

The anode wire was stretched along the axis of a cylindrical cathode with an inner diameter of 29 mm. The length of the wire was 90 mm. Figure 2-2 shows the position resolution (FWHM) against the input charge in terms of the number of electrons. In the beginning, the effect of electronic circuit noise on the position resolution was examined. As shown in the insertion, two lump resistors R/2 were connected in series. The resistance R was chosen so as to be equal to the resistance of the anode wire of the carbon fiber or that of a carbon-coated quartz filament. The input charge Q (=CV) was transferred through a capacitance C by applying a step functional voltage V from a pulse generator. The closed circles and the closed squares in the figure correspond to the cases in which the lump resistances R are equal to the resistance of the carbon fiber anode wire (38 kΩ) and that of the carbon-coated quartz filament (360 kΩ), respectively. The results agreed well with theoretical expression for relative position resolution[2-3]

$$\frac{\Delta x}{x} = k\frac{1}{QR^{1/2}} \tag{2-4}$$

where k is a constant. The effect of electronic circuit noise can be observed at the input charge around 10^8 electrons. The position resolutions for the Mn KX-rays are shown by open

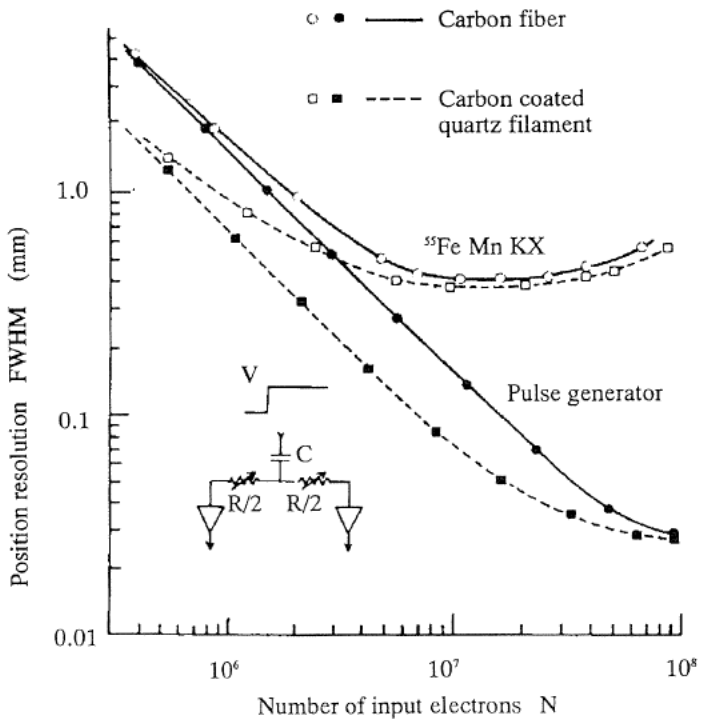

Fig. 2-2 Position resolutions for ^{55}Fe Mn KX-ray incidence (○, □) and pulse generator input (●, ■) as a function of input charge N in terms of number of electrons on carbon fiber: solid line, and carbon coated quartz filament: broken line.

circles for the carbon fiber and by open squares for the carbon-coated quartz filament. Better resolution for the latter is simply due to the larger resistance (see Eq. (2-4)). The gas gain increased with the voltage applied to the anode wire. The consequent larger input charge brought better position resolution. When the input charge exceeds 10^7 electrons, the resolution appears to be almost constant, because the collimator for the Mn KX-rays has the finite slit width of 0.39 mm and the Ar K photo-electrons ejected by the Mn KX-rays and the Ar K Auger electrons have their extrapolated ranges of about 0.5 mm in the counting gas. The best position resolution obtained for the Mn KX-rays was 0.42 mm, which was converted into 0.47% of the relative position resolution against the anode length of 90 mm.

The carbon fiber which we first applied to position-sensitive proportional counter (PSPC) can be used as a new resistive anode wire for charge division type proportional counters, although its commercial availability was confined to 7 μm in diameter and to about 4 kΩ/cm in electrical resistance. Because of the small diameter, a little caution is required for its handling and the energy linearity tends to be lost. The linearity and the resolution for the position of radiation incidence are satisfactory, which is the most important characteristics of position-sensitive detectors. The fiber is now used for PSPC in some research institutes in the world.

2.2.1.2 Partially resistive anode wire

In a coaxial cylindrical proportional counter as shown in Fig. 2-3(a), the electric-field strength at both ends of the anode wire is generally weak and the pulse heights are, therefore, smaller than those at the other parts of the wire as shown in (b), which is called the end effect. Because of this effect the counting efficiency decreases at the ends and, hence, it is necessary to know the effective volume contributing to the actual counting when the absolute value of the radioactivity of radioactive gaseous sample is to be known. If, however, a position-sensitive proportional counter (PSPC) is used, the position where a ^{3}H β-ray is detected can be found by the position signal.

The relation between the counts and the position signals is obtained as shown in Fig. 2-3(c). The total counts of pulses with position signal in the range **W'**, which is free from the end effect, come from the β-rays emitted from ^{3}H contained in the volume defined by the cathode wall and a geometrical length **W** shown in (a). Since ^{3}H β-rays have a penetration range r of about 1 cm in the counting gas with atmospheric pressure, it is necessary to confirm that the total counts in the position signal range **W'** shown in (c) come from ^{3}H contained only in the geometrical length **W** in (a). In a charge-division-type PSPC with a resistive anode wire connected with charge-sensitive preamplifiers, a position signal shows the average position[2-4] of the track weighted by the ion-pair density produced along the track by a corresponding β-ray. If ^{3}H gas density is uniform throughout the counter, the number of the position signals per unit length of the counter is constant. In this context, the coming and going of β-rays across the broken line shown in Fig. 2-3(a) is completely compensated, provided the broken line is distant more than the maximum range r of β-rays from the place

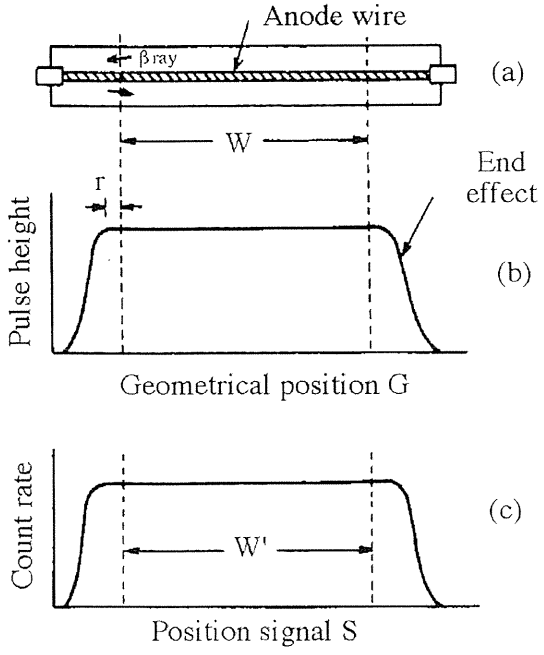

Fig. 2-3 Basic principle of the use of position-sensitive proportional counter for the elimination of end effect.

where the end effect disappears. It can now be stated that the total counts in the range **W'** shown in (c) come from the effective volume defined by the geometrical length **W** in (a). This is the new basic principle of the elimination of the end effect by use of a PSPC.

Figure 2-4 shows the relation between the position signal S ($= V_R/(V_L + V_R)$) and the geometrical real position G where β-rays are detected. Without lump resistors shown by A in Fig. 2-5(a), a linear relation (a) in Fig. 2-4 is obtained. Since the position resolution is proportional to the gradient (dS/dG) of the relation, the introduction of the lump resistors to avoid cutting off of ^3H β-ray signals by each discrimination level greatly deteriorates the resolution as shown by (b). In the case of Fig. 2-4(a), the position resolution will be about 0.5 ~ 1 mm for a charge-division-type PSPC with an anode length of, for instance, 50 cm. In Fig. 2-4(b), the resolution will be about 2 ~ 4 mm, which is not enough to accurately define the effective volume shown in Fig. 2-3(a). To overcome this difficulty, we introduced the new concept of a partially resistive anode wire.

To relate the effective volume with the count rate, the geometrical position of the broken line shown in Fig. 2-3(a) should be accurately related to the broken line in the position signal as shown in Fig. 2-3(c). As shown in Fig. 2-5(a), only the parts where the geometrical position should be related to the position signal must be resistive[2-5]. The relation between the geometrical position G and the position signal S is shown in Fig. 2-4(c). The position resolution, which is proportional to dS/dG is greatly improved.

When ^3H gas together with the counting gas uniformly fills the counter shown in Fig. 2-5(a), the relation between the count rate and the position signal S will now be obtained as Fig. 2-5(b). Since the part c-d of the anode wire shown in (a) is conductive, the ratio of the electric charges obtained from the left and right preamplifiers is constant even if β-rays are detected at different positions in the part c-d, and hence the same pulse height of the position

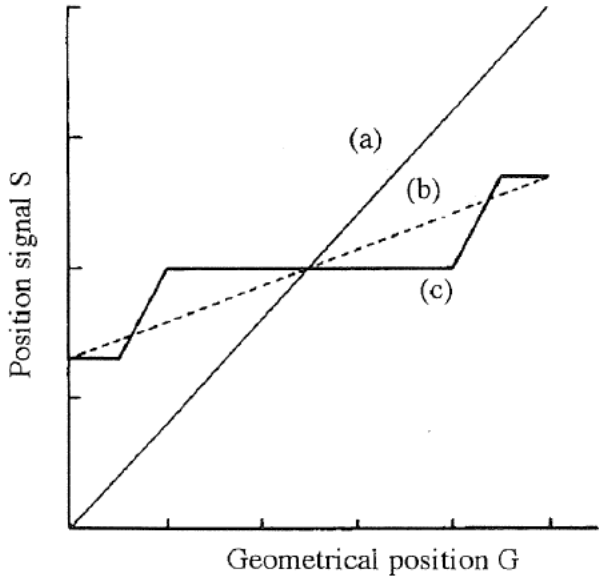

Fig. 2-4 Relation between position signal S and geometrical input position G on the resistive anode wire for the case (a) without lump resistors, (b) with lump resistors and (c) on a partially resistive anode wire with lump resistors.

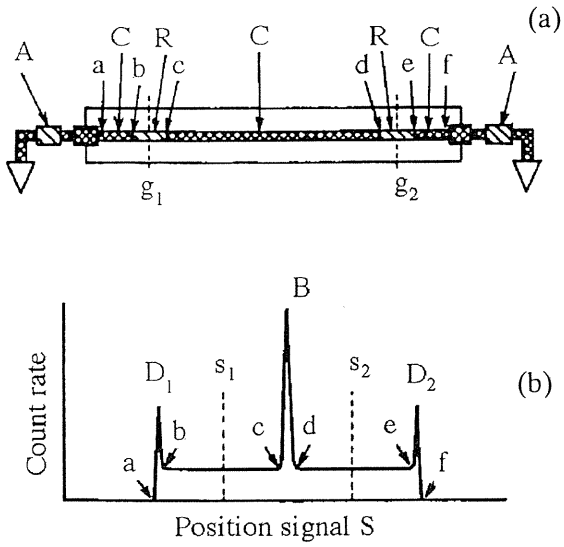

Fig. 2-5 Partially resistive anode wire to improve position resolution; A: lump resistor, C: conductive part, R: resistive part, and g_1, g_2: position calibration sources in (a). Count rate against position signal S (b).

signal is obtained. Consequently, the peak B in (b) will appear. The parts b-c and d-e in (a), however, are resistive, so that the pulse heights of the position signals depend on the actual positions where β-rays are detected in the resistive parts. Accordingly, the count rate distributes in the ranges b-c and d-c in (b). Therefore, if we experimentally confirm that when β-rays are detected at g_1 and g_2 in (a) the position signals appear at s_1 and s_2 in (b), respectively, it can be said that the total count rate in the range between s_1 and s_2 in (b) corresponds to the β-ray count rate in the volume defined by g_1 and g_2 in (a). The volume can be referred to as the effective volume. Thus, the radioactivity per unit volume in the counter can be accurately known. When the ratio of the effective volume to the total volume of the counter is known, the total radioactivity in the counter can be calculated. In this way, it is possible to establish a new method of direct activity measurement without the influence of the end effect.

An anode wire with resistive parts and conductive parts as shown in Fig. 2-5(a) must be made under conditions where the diameter is constant through the length. If conductive metal is vacuum-deposited on a resistive wire being covered partially with a foil, the covered part will remain as a resistive part. A Pyrex glass wire was suspended in a bell jar of a vacuum-deposition equipment. Chromium is very stable in various atmospheres and its specific resistance, 1.7×10^{-5} Ωcm, is large compared with other metals. The resistance of the wire after chromium vacuum deposition was about 20 kΩ/cm, which was appropriate for our purpose. Over a length of 5 cm, two parts of the wire were covered with aluminum foils and gold was vacuum-deposited on the other parts of the wire to obtain conductive parts. We determined a length of 5 cm taking account of the fact that the maximum range of ^{3}H β-rays in the atmospheric pressure of methane, is about 1 cm. The resistance of the conductive parts was about 100 Ω/cm which was 1/200 to that of the resistive parts.

The variation of the pulse height remains within ±15% over all the measurement of ^{3}H β-rays. The relation between the position signal S and the geometrical position G of X-ray

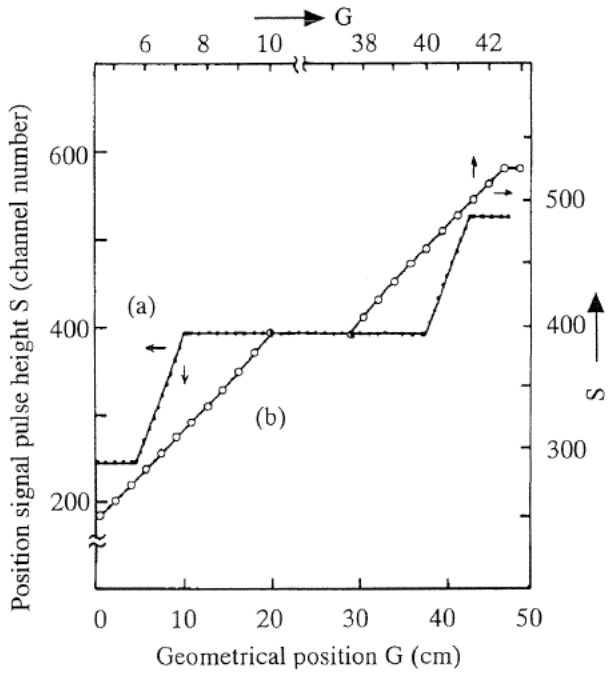

Fig. 2-6 Position signal pulse height S against the geometrical position G of the partially resistive anode wire.

incidence is shown in Fig. 2-6(a). In this case, the total resistance of the two resistive parts was 204 kΩ and two lump resistors A of 110 kΩ each were inserted as shown in Fig. 2-5(a). Since the resistances of conductive parts are very small, position signals with a constant pulse height were obtained irrespective of the geometrical position of X-ray incidence. The position signal at the resistive parts changed almost linearly with the X-ray incident position. This is shown more clearly in Fig. 2-6(b). On the whole, the uniformity of the resistances is satisfactory and does not affect the β-ray compensation at the boundaries of the effective volume. The collimated Mn KX rays were injected into PR gas at one of the resistive parts. The position resolution is 0.70 mm, which is also acceptable. If the anode wire is resistive over the full length, FWHM will be about 2 mm. The importance of the employment of a partially resistive anode wire would be recognized.

2.2.1.3 Logarithmic pulse amplifier

Figure 2-7 shows the block diagram of a PSPC system including a logarithmic amplifier, inserted between a linear amplifier and an ADC. In the logarithmic pulse amplifier, the following relation between the input linear pulse height v_i and the output pulse height V_o is valid, with constants α and β.

$$V_o = \alpha + \beta \ln(v_i). \tag{2-5}$$

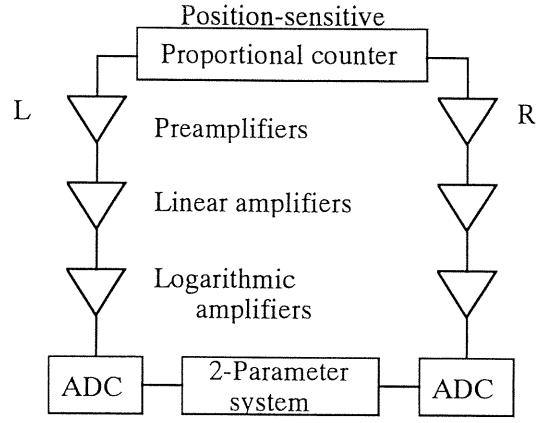

Fig. 2-7 Block diagram of the PSPC system with logarithmic amplifiers.

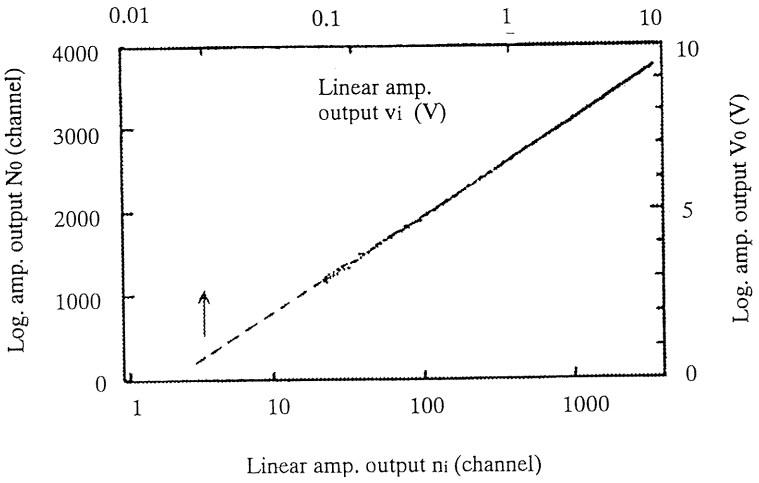

Fig. 2-8 Logarithmic-amplifier output vs. linear-amplifier output.

An analogous relation is given for the channel number n_i, converted for v_i through the ADC, and N_o for V_o with constants a and b:

$$N_o = a + b \ln(n_i). \tag{2-6}$$

Transforming eq. (2-6) inversely, a numerical value N_i corresponding to n_i, can be obtained by using N_o:

$$N_i = A \times B^{No}, \tag{2-7}$$

where $A = \exp(-a/b)$ and $B = \exp(1/b)$. The calculated numerical value N_i has more significant digits than the channel number n_i directly obtained through the ADC. For example, supposing the maximum value of v_i to be 10 V and the corresponding maximum channel number n_i to be 4096, the channel number n_i corresponding to v_i with a pulse height of less than 0.1 V will be less than 40 channels. However, the logarithmic output V_o corresponding to $v_i = 0.1$ V will be about 2 V and the corresponding channel number N_o will be about 1000 channels, which brings more significant digits in N_i than in n_i.

We used the temperature-compensated logarithmic operational element 759 N of Analog Devices. In the calculation of eq. (2-7), the constants a and b must be obtained beforehand through eq. (2-6). Figure 2-8 shows the relation between the linear-amplifier output v_i [V] or n_i [channels] and the logarithmic-amplifier output V_o or N_o. A channel number n_i of less than 30 or 40 was difficult to obtain because of the presence of the lower-level discrimination (LLD) of the ADC.

The position x of detected radiation versus the counter length L is obtained by

$$x/L = n_{iR}/(n_{iL} + n_{iR}), \tag{2-8}$$

where the suffixes L and R mean the left- and right-hand side, respectively, in Fig. 2-7. In the system with logarithmic amplifiers, however, the position is obtained through the following calculation using eq. (2-7):

$$\frac{x}{L} = \frac{A_R B_R^{N_{0R}}}{A_L B_L^{NL} + A_R B_R^{N_{0R}}} \tag{2-9}$$

Figure 2-9 shows the pulse-height distribution when methane labeled with ^{14}C was injected. The spectrum in Fig. 2-9(a) is that of the linear-amplifier output n_i showing the substantial difficulty to observe the pulses with low amplitude less than 0.1 V; Fig. 2-9(b) gives the logarithmic-amplifier output N_o showing the observation of a low pulse height with about 1 V of V_o which corresponds to a very low voltage of v_i, even less than 0.01 V, and the possibility of the clear setting of LLD of the ADC. The distribution in Fig. 2-9(c) is the linear spectrum N_i obtained by inverse transformation using N_o. The numerically obtained value N_i has at least three significant digits compared with n_i having an accuracy of only the channel number itself.

Figure 2-10 shows position spectra of ^{14}C β-rays. The spectrum in Fig. 2-10(b) was obtained just after the injection of methane labeled with ^{14}C into the counter through the central port. The labeled gas diffuses toward the counter ends at which the detection efficiency decreases by the end effect[2-1]. The measurement of β-ray counting during the time before the labeled methane reaching the ends ensures an almost 100% detection efficiency of the total radioactivity of the injected gas without the influence of the end effect. Therefore, this method can be used to measure the absolute radioactivity of gaseous samples and be named as "Diffusion method in long proportional counter". The position spectra after the complete diffusion of the labeled gas throughout the counter, by using a circulation pump, are shown in Figs. 2-10(c) and (d). The spectrum in Fig. 2-10(c) was obtained through the calculation with eq. (2-8) with the linear-amplifier output n_i shown in Fig. 2-9(a), in which the detection efficiency for pulses with low voltage was very poor and the erroneous position signal appeared because of the large digital error in the calculation of eq. (2-8) for a small channel number n_i corresponding to a low output voltage v_i, from the linear amplifier. Although there are several methods to avoid the error itself, degradation of the position resolution due to the

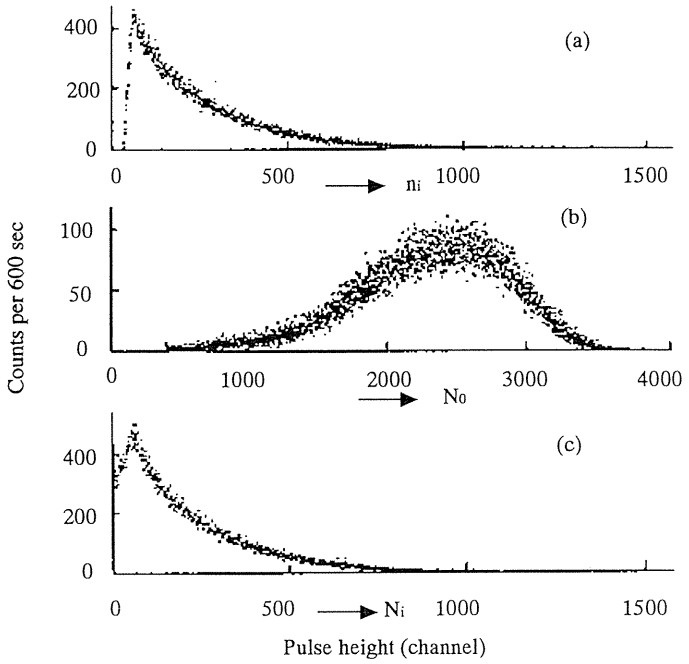

Fig. 2-9 Pulse-height spectra of ^{14}C beta-rays from (a) the linear amplifier and (b) the logarithmic amplifier, and (c) the calculated linear pulse height using (b) and eq.(2-7).

small channel number cannot be avoided. The spectrum in Fig. 2-10(d) was obtained through the calculation with eq. (2-9) with the logarithmic amplifier output N_o shown in Fig. 2-9(b). The detection efficiency is almost 100%, even for pulses with a low amplitude about 0.01 V, and there appears no digital error. The spectrum in Fig. 2-10(e) was obtained with three position calibration sources. The count rate in the area enclosed with the broken lines in Fig. 2-10(d), corresponding to the outer two sources, is multiplied by the ratio of the volume of the total counter system, including a circulation pump, to the volume enclosed by the positions of the outer two sources, and the result gives the total radioactivity of the injected gaseous sample[2-5,2-6]. The total radioactivity obtained by this method agreed with the result obtained in Fig. 2-10(b) within 1%.

2.2.1.4 One sided pre-amplifiers

(a) Rise time analysis

When one end of a resistive anode wire of a PSPC is grounded through a capacitor, a grounding capacitor hereafter, two components with different rise times are observed[2-7] in an output signal pulse from the other end. If the impedance of the grounding capacitor is much smaller than that of the anode, the amplitude of the fast component is proportional to a product of a distance x between the grounding capacitor and the position of an electron avalanche and the total charge generated by the electron avalanche. On the other hand the amplitude of the slow component is proportional to the total charge and is almost independent of

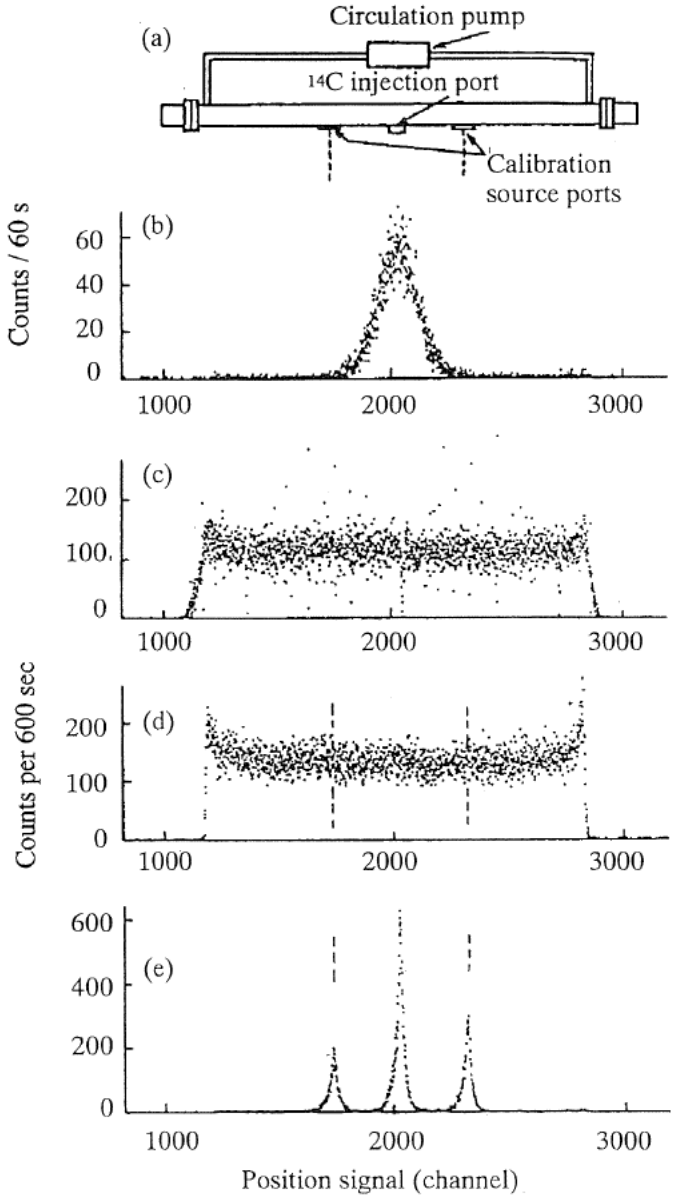

Fig. 2-10 (a) PSPC and (b) position spectra obtained with the logarithmic amplifier just after injection of ^{14}C-labeled methane, (c) obtained with the linear amplifier output after diffusion and (d) with the logarithmic amplifier out put, and (e) for three position calibration sources.

x. The rise time of the fast component is determined by the product of the resistance of anode wire and detector capacitance, the position of the electron avalanche[2-8], and/or the ion drift velocity. The rise time of the slow component, however, is mainly determined by the product of the anode-wire resistance and the capacitance of the grounding capacitor.

Figure 2-11 shows traces of output signals of a pre-amplifier connected to a resistor array simulating the counter (anode resistance is 7 kΩ, grounding capacitance is 2200 μF), when constant charge pulses with rise time of 25 ns from a mercury pulser were injected at x/L = 0.1, 0.5, 0.9 into the array. The amplitudes of the fast component, namely the amplitudes at about 0.5 μs, are nearly proportional to x/L. On the other hand, the amplitudes of the slow component, namely the amplitude at about 20 μs, are almost same regardless of the value of x/L. Therefore we can get information about x/L, i.e. the position of a radiation-induced event, through the division of the amplitude of the fast component by that of the slow one. In practice the division was performed by a calculation of V_f/V_s, where V_f and V_s are the output pulse heights of the linear amplifiers with fast and slow pulse shaping time constants, respectively.

Figure 2-12 shows a schematic view of a counter system. The counter consisted of a resistive anode wire, 7 kΩ, of Nichrome with a diameter of 15 μm and a brass cathode tube

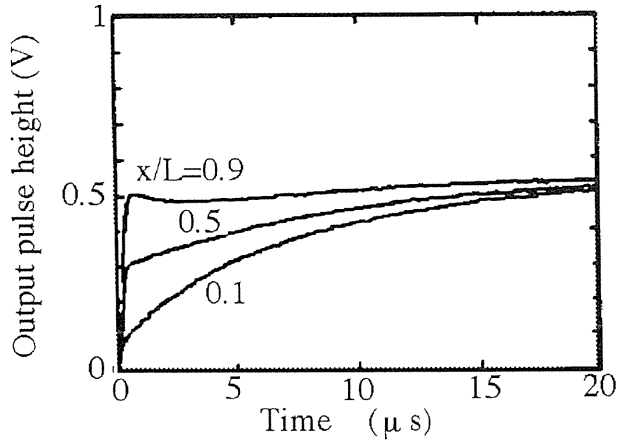

Fig. 2-11 Output pulses of preamplifier from an equivalent circuit simulating the proposed counter.

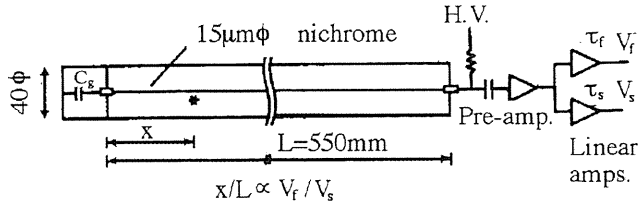

Fig. 2-12 Schematic view of the counter system. The asterisk shows the position of an electron avalanche.

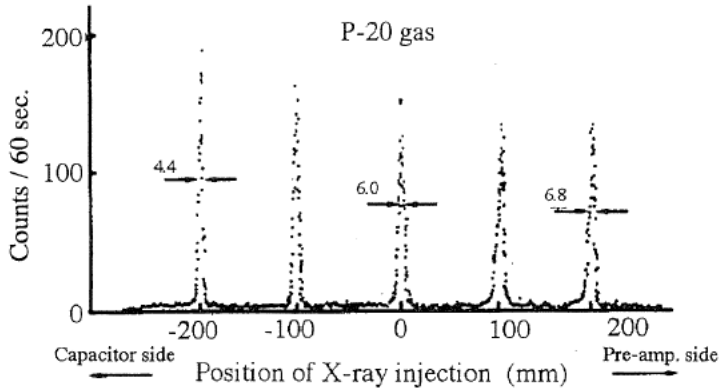

Fig. 2-13 Position profile obtained for Mn K X-rays at normal incidence when the counter was operated with P-20 gas.

with a length of 550 mm and an inner diameter of 40 mm. The anode wire was grounded at one end through the grounding capacitor C_g with 2200 pF and was connected to a pre-amplifier at the other end. On the upper side of the counter there was a window for X-ray injection with a length of 400 mm and a width of 10 mm made of aluminum-evaporated myler film with a thickness of 12 μm.

The output signals from the pre-amplifier were shaped and amplified by two linear amplifiers with pulse shaping time constants of 0.1 μs (ORTEC 579) and 10 μs (ORTEC 570). These time constants were chosen to obtain the best integral linearity. After converting these analogue signals to digital ones by 12 bits Wilkinson type ADCs, the position signals were obtained by dividing the former amplitude V_f by the latter one V_s. In this method, only a single pre-amplifier is needed.

Manganese KX-ray beams collimated to 0.4 mm from an ^{55}Fe source were injected perpendicularly to the counter axis. The position signals obtained are shown in Fig. 2-13, where the counter was operated with P-20 gas (Ar 80%, CH_4 20%).

The best position resolution was 4.4 mm, hence the relative position resolution was 8.0×10^{-3}, when the counter was operated with P-20 gas. The position resolution was better at the grounding capacitor side than at the pre-amplifier side. This position dependence is due to an error propagation in the calculation of V_f/V_s. Details were discussed in the reference[2-9]. Fairly sufficient linearity was observed over the effective length. The integral non-linearity was less than 0.5%.

(b) Coaxial double cathode

The counter consists of two coaxial cylindrical tubes and a resistive anode wire. The inner tube, cathode tube hereafter, works as a cathode of the counter and a collector of total charge signals. The outer tube, shielding tube hereafter, works as an electrostatic shield and a mechanical cover. By applying an appropriate positive high voltage to the anode wire, the counter works as a proportional counter. The one end of the resistive anode wire is grounded through a grounding capacitor C_g. With large capacitance of the grounding capacitor C_g, the impedance of the capacitor for signal pulse becomes sufficiently small. In this condition, Q_a, which is an output of a linear amplifier with an appropriate pulse shaping time constant

following a charge sensitive pre-amplifier connected to the anode wire at the opposite side of the grounding capacitor, is proportional to the distance x from the grounding capacitor to the position where an electron avalanche occurred. Therefore Q_a is expressed as eq. (2-10), where Q_t represents a total charge produced by an electron avalanche, L is a length of the resistive anode wire and $\eta_a(x)$ is explained below. On the cathode tube, a charge which is proportional to the total charge Q_t is induced so that the output Q_C of a linear amplifier is expressed as eq. (2-11). The output Q_C does not depend on a position of a electron avalanche.

$$Q_a = (x/L) \cdot \eta_a(x) \cdot Q_t \tag{2-10}$$

$$Q_C = -\eta_C \cdot Q_t \tag{2-11}$$

where $\eta_a(x)$ and η_C are effective charge collection efficiencies due to ballistic deficit at the pulse shaping of the linear amplifiers following pre-amplifiers which are connected to the anode wire and the cathode tube. Though $\eta_a(x)$ depends on the position of an electron avalanche, it can be treated as a constant value by choosing a pulse shaping time of a linear amplifier to be long compared to a rise time of a signal. In this experimental situation we, therefore, treated $\eta_a(x)$ as a constant value. It is evident from eqs. (2-10) and (2-11) that the position information of an electron avalanche can be obtained as a value being proportional to x/L by calculation of Q_a/Q_C.

The counter consists of a resistive anode wire of Nichrome with a diameter of 15 μm and coaxial tubes of stainless steel with a thickness of 0.5 mm. The length and the inner diameter of the shielding tube (outer tube) are 1300 mm and 25 mm, and of the cathode tube (inner tube) are 1240 mm and 23 mm. The tubes are insulated each other at the end of the cathode tube by Teflon spacers. The total length and resistance of the anode wire including a leading wire section are 1300 mm and 7 kΩ, respectively. The one end of the anode is grounded through the grounding capacitor C_g. The capacitance of the grounding capacitor was decided to be 2200 pF from a calculation[2-9] to satisfy considerable integral linearity. A charge sensitive pre-amplifier is connected on the other end of the anode wire.

Gas mixture of ^{3}He and CF_4 (^{3}He 30% + CF_4 70%) was used as a counting gas which is prominent for a position sensitive counter of thermal neutrons[2-10].

2.2.1.5 Noise reduction

The two output signals obtained from both sides of the PSPC include the inversely correlative thermal noise component, which is mainly generated in the anode wire and the first stage FETs of the pre-amplifiers. This noise mainly arises from thermal vibration of electrons in the resistive anode wire and the fluctuation of drain current due to the depletion layer fluctuation in the channels of the first stage FETs. The inversely correlative noise component between the left output $V_L(t)$ and the right one $V_R(t)$ is observed. The thermal noise of each output has the same amplitude. The thermal noise $\Delta(t)$ can be obtained by using the inversely correlative characteristic between the left and the right outputs as Eq.(2-12);

$$\Delta(t) = \frac{V_L(t) - V_R(t)}{2} \tag{2-12}$$

To reduce the thermal noise in the output signals[2-11,2-12], the thermal noise component or $\Delta(t)$ is subtracted from the left output $V_L(t)$ and added to the right output $V_R(t)$ as follows;

$$V_L'(t) = V_L(t) - \Delta(t) \tag{2-13}$$

$$V_R'(t) = V_R(t) + \Delta(t) \tag{2-14}$$

where $V_L'(t)$ and $V_R'(t)$ are the output signals after reducing the thermal noise component.

Practically, the amplitude of the pulses from both outputs are no longer equal depending on the incident position of radiation onto PSPC. The output signals from the equivalent circuit are shown in Fig. 2-14 when charge pulses are put into the resistor array near the left terminal by a mercury pulse generator. For these general cases, the above noise reduction method can not be directly applied and eqs. (2-12) ~ (2-14) should be modified as follows.

It is noted that the slope of leading edge, as well as the amplitude, of the pulse strongly depends on the position[2-13] where a signal arises. The slope of leading edge is proportional to the relative position. The incident position can practically be obtained by the ratio of the slope of leading edge of signals. Here is introduced a factor k, which is the ratio of the slope of leading edge of the left output signal to that of the right and decided at every sampling data;

$$k = \left(\frac{dV_L(t)}{dt}\right) \Big/ \left(\frac{dV_R(t)}{dt}\right) \tag{2-15}$$

To extract the thermal noise components from both output signals, the right output signal multiplied by k, $kV_R(t)$ is subtracted from the left output signal $V_L(t)$. The amplitude of $kV_R(t)$ is equal to that of $V_L(t)$ in the amplitude over the rise time of the leading edge. Because the amplitude over the rise time of the leading edge is inversely proportional to the relative position. Therefore, only thermal noise component can be reduced without affecting the rise time of leading edge which includes an important information on the position. In this case, a thermal noise component $\Delta(t)$ is given by Eq.(2-16);

$$\Delta(t) = \frac{1}{k+1}\left(V_L(t) - kV_R(t)\right) \tag{2-16}$$

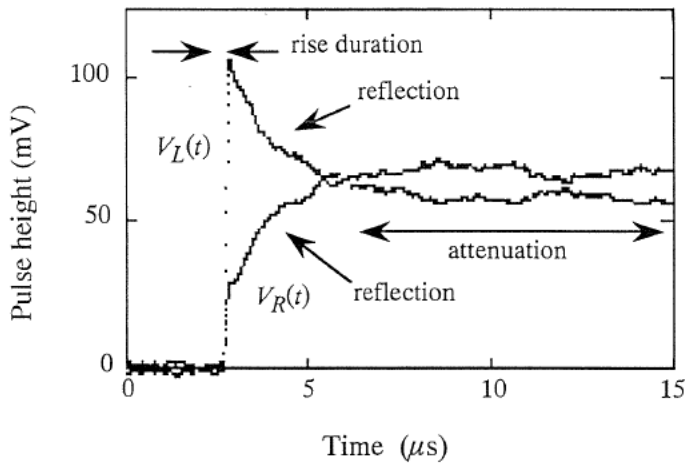

Fig. 2-14 The output signals of the equivalent circuit simulating the PSPC.

By substituting Eq. (2-16) into Eqs. (2-13) and (2-14), the thermal noise component is reduced from the signals. This noise reduction method is named the *kΔ-method*. The *kΔ-method* can simultaneously reduce the reflection of signal produced at each end of the PSPC, which appears as the rising and attenuating components after the steep slope of leading edge of each output signal of $V_R(t)$ and $V_L(t)$ in Fig. 2-14.

Even after the *kΔ−method* procedure, there remains white noise. In order to obtain a better signal to noise ratio, the digital filtering has been applied to the signals corrected by the *kΔ-method* through a convolution integration. The output signal $f_0(t)$ is obtained by a convolution between the signal $f_s(t)$ and the impulse response function $h(t)$ of a filter as shown in Eq.(2-17);

$$f_0(t) = \sum_{k=-\infty}^{\infty} f_s(t-k) \cdot h(k) \tag{2-17}$$

In this work, two kinds of digital filter were tried, one is a CR-$(RC)^4$ filter that consists of a single stage of CR differentiator and four stages of RC integrator and the other is a finite cusp filter that shows the best signal to noise ratio among practical filters[2-14]. The pulse shape after the CR-$(RC)^4$ filtering is very similar to a true Gaussian shape that has a relatively good signal to noise ratio. The finite cusp filter is difficult to realize by analog circuits, but the digital waveform processing makes it without any problems.

The impulse response function $h_{CR}(t)$ for the CR-$(RC)^4$ filter, and $h_{C1}(t)$ and $h_{C2}(t)$ for the cusp filter are given in Eqs. (2- 18) ~ (2-20).

$$h_{CR}(t) = \frac{t^3}{\tau^4}\left(\frac{1}{3!} - \frac{t}{4!\tau}\right) e^{-\frac{t}{\tau}} \tag{2-18}$$

$$h_{C1}(t) = \delta_I(t) - \frac{1}{\tau}\, e^{-\frac{t}{\tau}} \tag{2-19}$$

$$h_{C2}(t) = -e^{\frac{t}{\tau}} \tag{2-20}$$

where τ is the time constant, and $\delta_I(t)$ is the Dirac's delta function.

The block diagram of the digital waveform processing system is shown in Fig. 2-15. The principal components of this system are detector with two following pre-amplifiers, a transient converter and a computer system.

The PSPC or an equivalent circuit simulating PSPC was used as a detector. One of the PSPC was consisted of a cylindrical cathode tube with an inner diameter of 29 mm and an anode wire made of Nichrome with a resistance of 1.3 kΩ, a diameter of 10 μmϕ, and a length of 12 cm. There is an entrance window with a length of 6 cm for X-ray injection. The equivalent circuit simulating the PSPC had a series of 13 resistors of 100 Ω each as a substitute of the resistive anode wire. The charge-sensitive pre-amplifiers were connected to both outputs of the detector.

The transient converter that had a 9 bit resolution and sampling rate of 100 MHz followed the pre-amplifiers to acquire the outputs as discrete digital signals. The transient converter had two input terminals. The position resolution was also evaluated for comparison with a conventional analog processing method. The position resolutions obtained with the digital and analog processing were compared by using the PSPC signals for a collimated ^{55}Fe X-ray beam with a width of 0.4 mm.

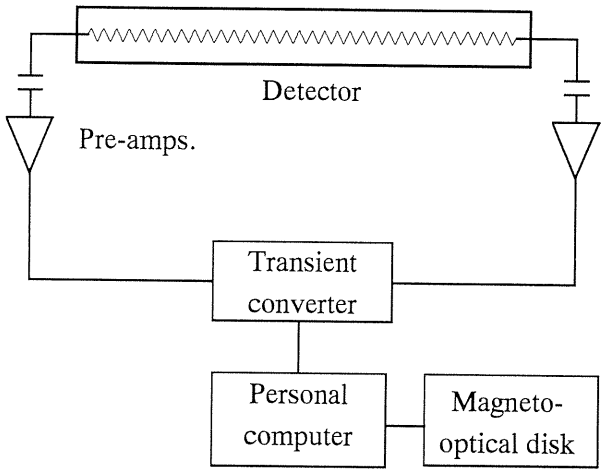

Fig. 2-15 Schematic diagram of the digital processing system.

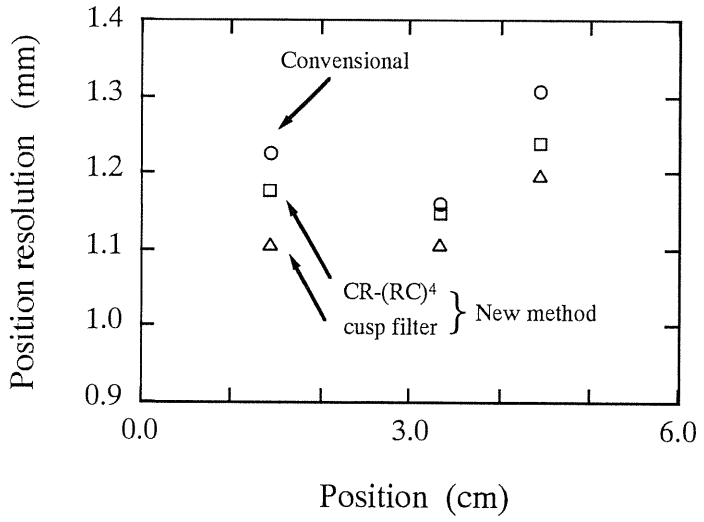

Fig. 2-16 Position resolutions of the PSPC. ○: Analog filter, □: *kΔ-method*, Digital CR-RC^4 filter, △: *kΔ-method*; Digital cusp filter.

The ^{55}Fe X-ray beam was entered into the PSPC through the incident window. A counting gas was PR gas. The applied voltage of 1380V was determined to obtain the best position resolutions. The pre-amplifier output signals were shaped by the digital filers with the *kΔ-method* or the linear amplifiers.

Figure 2-16 shows the position resolutions defined by the FWHM. The shaping time constants were 1 μs at which the best position resolutions were obtained. The position resolu-

tions obtained with the digital waveform processing were improved 4 ~ 5% in the CR-$(RC)^4$ filter and 8 ~ 10% in the cusp filter in comparison with those obtained by the analog filter.

2.2.1.6 Position sensing with neural network algorithm

The position information was obtained directly from the pulse shape. The typical pulse shapes of events at three positions has been shown in Fig. 2-11. If the difference among the pulse shapes can be recognized, the position information can be obtained. The neural network was used for recognition of the pulse shape.

A three layered feed forward type neural network was adopted as the position sensing algorithm. The schematic diagram of the neural network is shown in Fig. 2-17. The first layer consisted of forty neurons as input units and a neuron as a bias unit. The digitized amplitudes of pre-amplifier output signals, averaged for every 200 ns, were fed to the input units. The second layer consisted of eight neurons as hidden units and a neuron as a bias unit. The third layer consisted of one neuron as an output unit. The output stage provided the position of radiation interaction in the PSPC.

The output of each neuron was transferred to the next neurons weighted by the value of synapse that was the bridge between two neurons. An error back-propagation algorithm was adopted for a learning rule[2-15]. With this algorithm, the neural network repeatedly examined the pulse patterns and corrected each weighting value of synapse by the back-propagation of the error of output value. The learning data for the error back-propagation algorithm was made by averaging pulse shape of the same position to reduce fluctuations due to electronic noise. The learning data consisted of twenty-one pulse shapes at 2 cm intervals from the center of the injection window of the PSPC. After the optimization process, the neural network recognized each pulse shape and provided the position of radiation interaction.

Manganese K X-ray beams collimated to 0.4 mm width from an ^{55}Fe source were perpendicularly injected at 5 cm intervals through the injection window provided on the cathode wall. The pulse shapes from the pre-amplifier of the PSPC were digitized with the transient converter. We obtained position profile by putting the digitized pulse shapes into the optimized neural network as mentioned above. The position distributions at 5 cm intervals from the center of the injection window of the PSPC are shown in Fig. 2-18(a). The best position

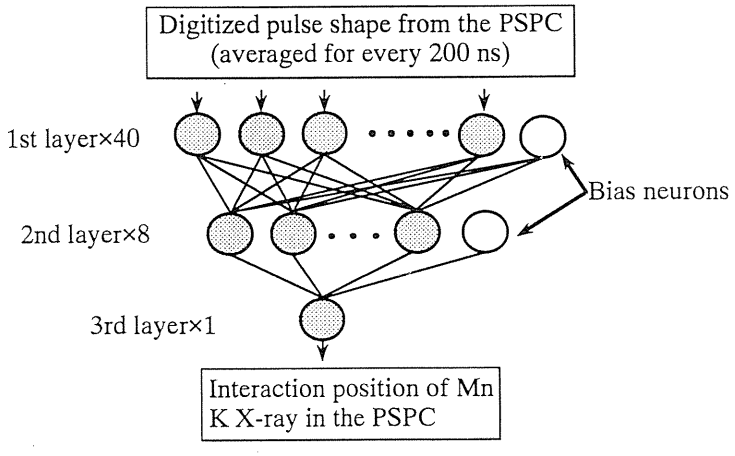

Fig. 2-17 Schematic illustration of the neural network.

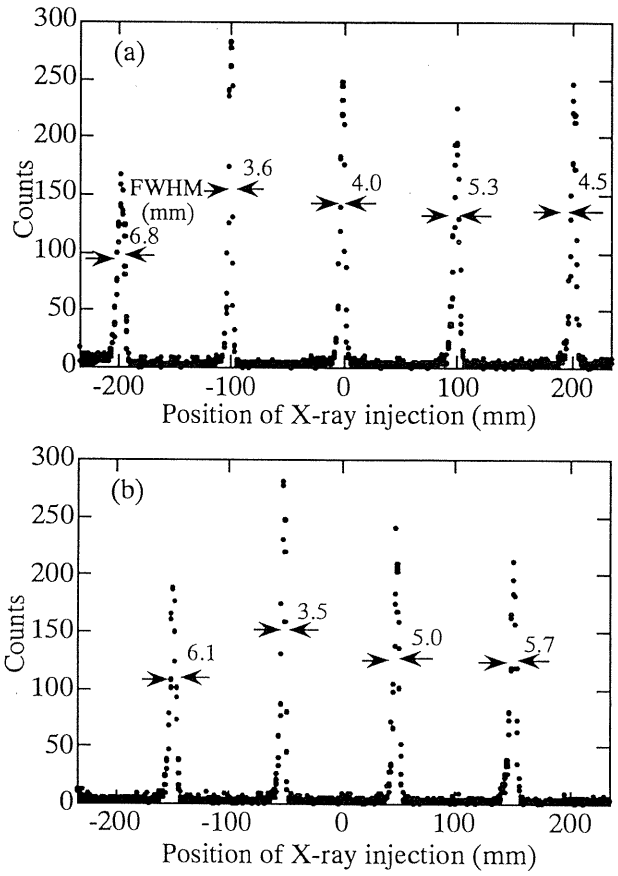

Fig. 2-18 Position distributions obtained for Mn K X-rays at (a) ±0 cm, ±10 cm and ±20 cm, (b) ±5 cm and ±15 cm, from the center of the injection window.

resolution was 3.5 mm, or the relative resolution of 6.4×10^{-3}, and the integral nonlinearity of the position signals was less than 0.3%. The learning data we used were the averaged pulse shapes at 2 cm intervals from the center of the injection window. Therefore the neural network was optimized without the pulse shapes at ±5 cm and ±15 cm from the center. However, the measured data showed good position resolutions and good linearity even for non-learned positions that were shown in Fig. 2-18(b). The results of this new method were an improvement over those obtained with the previous analog method in which the best relative position resolution was 8.0×10^{-3} [2-16,2-17].

2.2.2 *Applications to absolute radioactivity measurement*

It is possible to measure the movement of radioactive gas introduced into a PSPC. When the radioactivity of gaseous sample is determined using proportional counter, there is so-called end effect to suffer from. Only one method to avoid the effect is length-compensation method developed by Mann et al.[2-18] which has been widely used over the world. The method however needs more than two counters. We found two new methods to use PSPC for

the absolute measurement of gaseous samples. One is "diffusion in a long counter method" and the other is "position-sensitive proportional counter method". The former has been adopted in Japan Atomic Energy Research Institute and Power Reactor and Nuclear Fuel Development Corporation.

2.2.2.1 Tritium

Figure 2-19 shows the structure of the position-sensitive proportional counter for the specific-activity measurement of ^{3}H-labeled methane. The cathode with an inner diameter of 40 mm has three ports. The central port is used for the injection of ^{3}H-labeled gas and the other two are used for the insertion of ^{3}H solid sources for position calibration. The anode wire with a diameter of 41.7 μm was properly positioned so that the center of each resistive part with a length of about 5 cm and resistance of 102 kΩ was situated at each position of two calibration ports. Since the outer end of the resistive part is about 55 mm distant from the tip of the electrode sleeve, the position of the resistive part, therefore, is almost free from the influence of the end effect. To obtain a uniform detection efficiency over most of the entire length of the anode wire, a lump resistor of I 10 kΩ was inserted between anode wire and each preamplifier.[2-19)]

^{3}H-labeled methane of about 1 cm^3 was injected into the counter through the central port and was diffused throughout the whole counter volume by the use of a pump. As shown in Fig. 2-20(a), when the applied voltage was 2.65 kV the pulse-height distribution is similar to ^{3}H β-ray-energy spectrum. But it is difficult to count all the β-rays with this pulse-height distribution. Moreover, a weak charge due to the small gas-multiplication factor brings poor position resolution. With a higher applied voltage of 3.65 kV, the gas multiplication for β-rays with higher energy is small[2-4)] and the pulse-height distribution has a peak as shown by (b). Noise pulses, however, due to perhaps single electrons, appear and such pulses must be discriminated. The lower level of pulse height selector (PHS) as shown by an arrow in Fig. 2-20(b) was set. The ^{3}H β-ray count rate was measured as a function of the lower level of the PHS and the change in the count rate due to the uncertainty of the lower level setting was found to be less than ±0.5%. When ^{3}H β-rays near the counter cathode make their tracks toward the cathode wall, the β-rays lose small amounts of energy and the resulting pulse height is small, which is the wall effect. The influence of this effect is very large in measurements with ionization chambers. In the counting method, however, this influence can be neglected by setting appropriately the lower level of the PHS, especially in the case of the pulse-height distribution shown in Fig. 2-20(b).

The distance between the centers of the left and right port was 330.40 ± 0.070 mm, measured by vernier calipers. The effective length needed for the determination of the effective volume was, therefore, 330.40 ± 0.11 mm including the error in the position determination at the resistive parts. The inner diameter of the cathode was 40.00 ± 0.05 mm. The effective volume without end effect could be determined as 415.2 ± 0.5 cm^3 with a relative error of

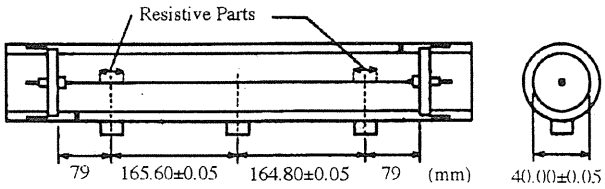

Fig. 2-19 Position-sensitive proportional counter with a partially resistive anode wire.

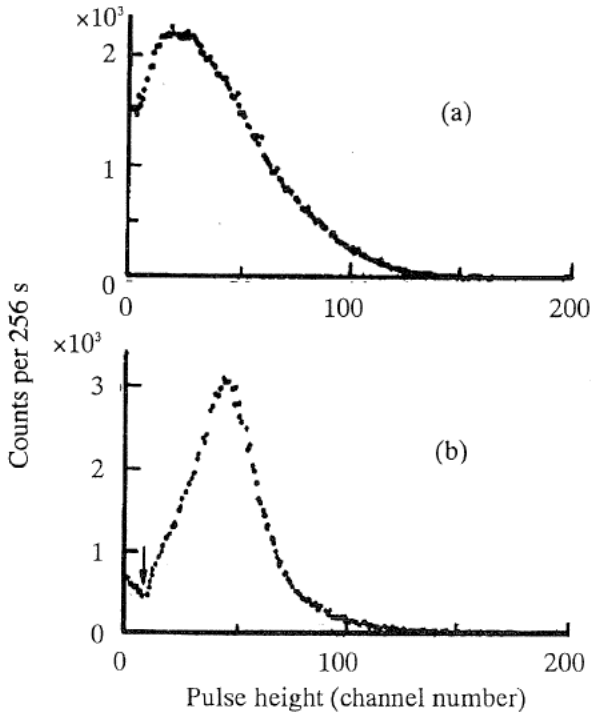

Fig. 2-20 Pulse-height distribution s of ^{3}H β-rays observed with an applied voltage of (a) 2.65 kV and (b) with 3.65 kV.

±0.12% (standard deviation). The change in the length of the cathode due to temperature change was negligibly small.

There are two quantities related to a radioactive gas to be measured; one is the total activity in the injected gas and the other is the activity per unit volume, or mole, in the counter.

Figure 2-21(a) shows the position spectrum with position calibration sources. The peaks c_1 and c_2 show the positions of the calibration sources which are the edges of the effective length of the anode wire. The peaks D_1, D_2 and B are the background counts at the conductive parts of the anode wire. The position calibration sources were taken out and ^{3}H-labeled methane with a volume of 1.1 cm^3 was injected through the central port. Figure 2-21(b) shows the position spectrum measured for 5.12 s after the injection. As it took time for the diffusion of the ^{3}H-labeled gas from the conductive part B to the conductive part D_1 and D_2 shown in (a), there are, as seen in (b) negligibly small counts at the positions corresponding to D_1 and D_2 when the background counts are subtracted. The total count in the region shown by the broken lines, therefore, corresponds to the total activity of the injected ^{3}H-labeled methane, although the error is rather large due to the short measuring time. The total activity was 125 ± 4 Bq.

The ^{3}H-labeled gas was circulated through the pump for 8 min and the position spectrum was measured. The gas was again circulated and the spectrum was measured as shown in Fig. 2-21(c). Both spectra were the same, which meant that the ^{3}H-labeled gas was uniformly diffused throughout the counter. From the total counts after subtracting the

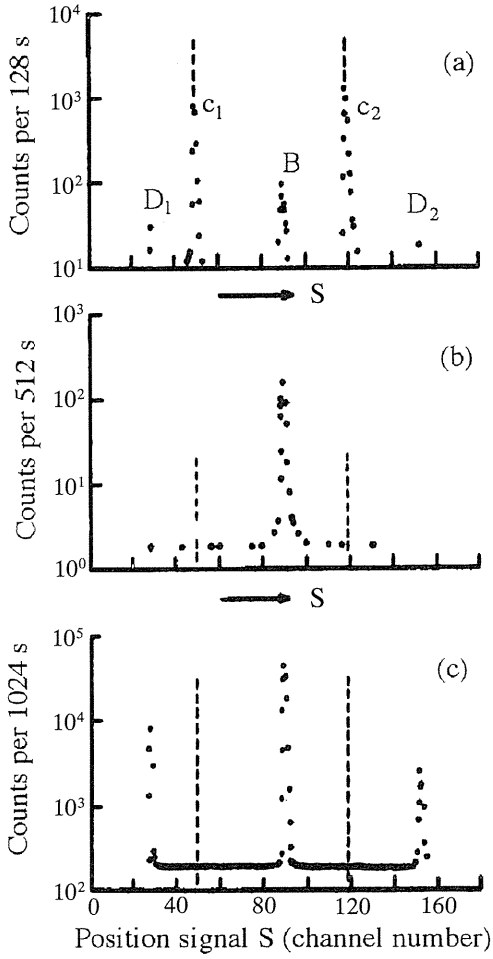

Fig. 2-21 (a) Position spectrum with two position calibration sources, (b) that of 3H-labeled methane measured for 5.12 s just after the injection and (c) that for 1024 s after complete diffusion.

background counts in the range between the broken lines and the effective volume as previously measured, the activity in the unit volume of the counter was found to be $202.5 \pm 1.6\,\mathrm{mBq/cm^3}$ with a tentatively estimated uncertainty of $\pm 0.79\%$ (standard deviation).

The total volume of the counter including the pumping system was calculated from the drawing shown in Fig. 2-19 and was $626\,\mathrm{cm^3}$. The total activity injected into the counter was 127 ± 4 Bq, which was similar to the value of 124 ± 4 Bq determined preliminary. When the total activity is to be determined precisely, the total volume of the counter system should be determined more accurately by measuring the pressure change or specific-activity change after connecting the total counter system to a container whose volume is accurately known.

Further important things to do are to make the effects of the discrimination level and the wall of the counter clearer, and also to make a comparison with standard samples calibrated by other methods.

To find the radial movement of ^{3}H-labeled gas, a multielement position-sensitive proportional counter was constructed[2-20].

2.2.2.2 Carbon-14

There are a few problems for ^{14}C β-rays in comparison with ^{3}H β-rays. The maximum penetration range of ^{14}C β-rays is about 40 cm in methane gas (1 atm., 20°C), whereas that of ^{3}H β-rays is only 0.82 cm. This difference brings the first problem with the pulse-height spectra. When an appropriate high voltage is applied to the anode wire, a desirable pulse-height spectra can be obtained for ^{3}H β-rays as shown in Fig. 2-20(b) (due to the effect of dE/dx on the gas multiplication factor[2-4,2-5] for β- rays with large energy. However, since the saturation phenomenon does not favorably work for ^{14}C β-rays with high energy due to their very long penetration ranges, there appear very large pulses, or in other words there appear many small pulses relative to the largest pulses for ^{14}C β-rays in any applied voltage. Therefore, the pulses whose amplitudes are less than the discrimination level are not counted. On the other hand, if a main amplifier with a large gain is used, β-rays with very low energy can be counted. However, pulses saturated in the amplifier appear and the correct position signals can not be obtained. It must be pointed out that the saturation of gas multiplication factor in the counter is favorable, but the non-linearity in the amplifier should be avoided.

One of the solutions for this problem is the introduction of two kinds of main amplifiers[2-21] with low and high gains after each of left and right preamplifiers as shown in Fig. 2-22(a). Only the left side is shown in the figure. For large signals from preamplifiers, main amplifiers with low gain are used so as to be able to obtain correct position signals by processing linear signals without pulse-height saturation in the main amplifiers. Since an analogue processor to yield position signals has a tendency to give inexact position signals for input signals with very small pulse height, amplifiers with high gain are used for small signals from preamplifiers to obtain exact position signals. As shown in Fig. 2-22 (b-2), the lower discrimination level (broken line C) of a pulse-height selector (PHS) for pulses from a low-gain amplifier was set at far lower level than that (broken line B′) corresponding to the higher level (broken line B shown in Fig. 2-22(b-1)) for pulses from a high-gain amplifier. The following selection for main amplifiers was performed through electronic switches between main amplifiers and a position-signal processor. When both left and right signals drop in the windows (A ~ B in (b-1)) of PHS's for signals from high-gain amplifiers, signals from high-gain amplifiers are chosen. For any other cases, signals from low-gain amplifiers are chosen, because it is necessary to send linear signals without pulse-height saturation in main amplifiers to the processor for obtaining correct position signals.

The second problem is the distance between the position calibration source and the end of the counter. This distance for ^{14}C β-rays must be much larger than that for ^{3}H β-rays to obtain an equilibrium of position-signal intensities around the boundaries of the defined volume. Although a simple calculation showed that a length less than a half of the maximum range of β-rays was enough for the present purpose, we tentatively chose a length nearly same as the maximum range of ^{14}C β-rays.

Figure 2-23 shows the drawing of the counter. A nickel-chromium alloy wire with a diameter of 20 μm, a length of 950 mm and a resistance of 2.09 kΩ was stretched along the axis of a stainless steel cylinder with an inner diameter of 40.0 ± 0.07 mm. At a center of the axial direction there is a port for the injection of radioactive sample gas and for the injection of a position calibration source of ^{14}C. Two hatches are attached and the position calibration

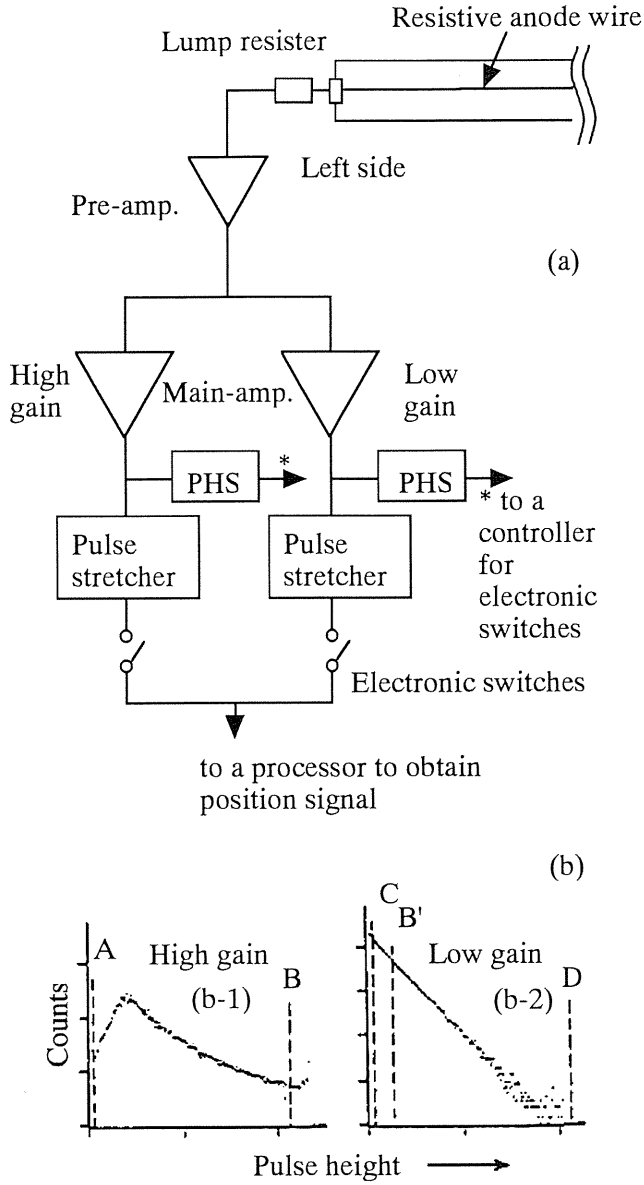

Fig. 2-22 Block diagram (a) of electronics having two main amplifiers with low and high gains for each pre-amplifier and the output pulse height spectra (b) from each amplifier.

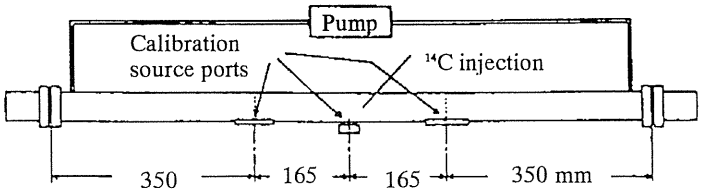

Fig. 2-23 Schematic of the counter.

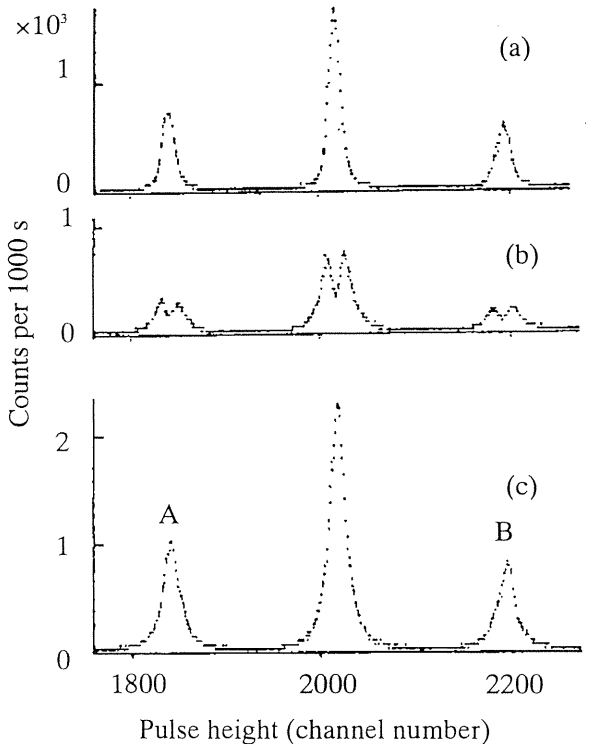

Fig. 2-24 Position signal spectra obtained with three position calibration sources; (a) obtained from high-gain amplifiers, (b) from high-gain amplifiers and (c) from both low- and high-gain amplifiers.

sources of ^{14}C can be mounted on the inner surfaces at positions of 164.9 ± 0.15 mm from the center. Hereafter, systematic error is expressed by the maximum conceivable systematic error. The defined volume can be determined to be 414.4 cm^3 with $\pm 0.88\%$ error. Methane was used as counting gas at the atmospheric pressure and a pump was used for the circulation of the counting gas. The total volume was calculated to be $1320\ cm^3 \pm 0.9\%$. A lump resistor with a resistance of 2.2 kΩ being nearly same as that of anode wire was fixed at each end of the wire. The two resistors were necessitated to obtain a detection efficiency with nearly a hundred percent over most of the anode wire[2-19]. The applied voltage was 3.2 kV.

With three position calibration sources shown in Fig. 2-23, the position-signal spectra were obtained as shown in Fig. 2-24 (a) through the high-gain amplifiers, (b) through the low-gain amplifiers and (c) through both high- and low-gain amplifiers. The split of the peaks in (b) can be explained as follows. The β-rays emitted perpendicularly to the anode wire are not able to cause large pulse height due to the short path length and therefore they can not drop in the PHS channels for low-gain amplifiers. As a results, a hollow shape appears at the position of the position calibration source. The distance between two peaks A and B in (c) could be determined with ± 2 channel maximum conceivable systematic error including the drift with time, which corresponds to ± 1.84 mm for geometrical length of the counter and to ± 0.56 for the volume defined by the dotted lines in Fig. 2-23.

Figure 2-25 (a) shows a position spectrum measured for twenty seconds just after the injection of ^{14}C-labeled methane of about 0.1 cm^3 through the central port of the counter. Since the total amount of the labeled gas was considered to remain in the central portion of the counter, all β-rays would be counted without the influence of the end effect and the total radioactivity was obtained to be 285.0 ± 4.5 Bq.

A pump located outside the counter circulated the radioactive gas. After about 20 minutes, the gas was uniformly distributed and a position spectrum was obtained by measuring for 1000 seconds as shown in Fig. 2-25 (b). Radioactivity concentration of the counting gas was obtained to be 215 ± 2.4 mBq/cm^3 by the count rate in the defined area between A and B. The ratio, 3.185 ± 0.0032, of the total volume of the counter including the pumping system to the defined volume gives the total activity of 283.9 ± 3.1 Bq which agreed with the activity of 285.0 ± 4.5 Bq obtained just after the injection.

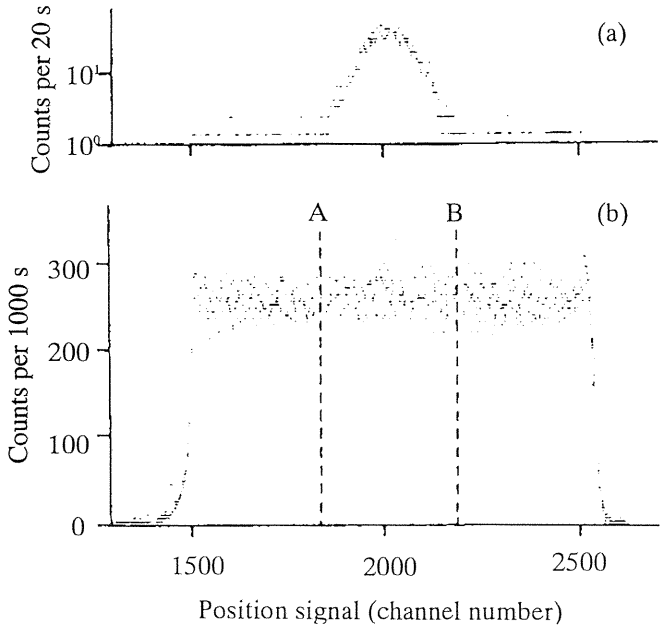

Fig. 2-25 Position spectrum for ^{14}C-labeled methane obtained by 20 s counting; (a) just after the injection of the labeled methane at the central port; (b) Position spectrum obtained by 20 minutes gas circulation with a pump.

In the position spectrum in Fig. 2-25 (b) there appear peaks near the counter ends, which arise from the following fact. Radioactive gas being present in the insensitive regions at both ends can emit β-rays toward the direction of the sensitive region and the β-rays detected give position signals around the peaks. The length, between a calibration source and the counter end, being necessary for ^{14}C activity counting in the present method has to be enough to obtain uniform count rate in the effective counting region. We tentatively considered that about 12 cm which was less than one-third of the maximum penetration range, 40 cm, of ^{14}C β-rays would be enough for the present purpose.

2.2.2.3 Krypton-85

In the case of ^{85}Kr, we had to use logarithmic amplifier. Figure 2-26 shows position spectra. Through the central port in Fig. 2-26(a), ^{85}Kr mixed with methane was injected and immediately measured. The position spectrum claculated using eq. (2-9) is shown in Fig. 2-26(b). Since ^{85}Kr had not yet diffused to the counter ends, there was no counting loss due to the end-effect. Under this condition, the total radioactivity could be determined for 60 s without the influence of the end-effect. We call this method the diffusion-in long proportional counter (DLPC) method. After this measurement, the counting gas was circulated with a pump to obtain a uniform distribution of ^{85}Kr throughout the counter. Figure 2-26(c) is the position spectrum calculated using eq. (2-8) for n_i obtained by connecting linear amplifier outputs to ADCs. Since there were many small pulses, there were clearly digital errors in calculations with eq. (2-8). Figure 2-26(d) is the spectrum claculated using eq. (2-9) and N_o obtained by connecting logarithmic amplifiers to ADCs. Digital errors disappeared and the count rate was larger than Fig. 2-26(c), since nearly all of the pulses were counted. The reason why the intensity at both ends of the spectrum is larger than that at the central part is explained as follows. As an example, the left end of spectrum in Fig. 2-26(c) is taken. The left peak situates at the end of the sleeve tube of the electrode. When ^{85}Kr between the left end-wall of the counter and the end of the sleeve tube emits a β-ray toward the end-wall, it will not be detected. On the other hand, when ^{85}Kr emits a β-ray toward and beyond the sleeve end, it will be detected and have a tendency to give a position signal around the peak. Similar phenomena can be expected for ^{85}Kr in the right-side region of the same sleeve end. In the central part, the flat region of the intensity can be seen with-out the influence of the end effect, which means that the compensation of β-rays going-out and coming-in at any position is accomplished. Figure 2-26(e) is the spectrum obtained with three position calibration sources inserted into three ports. The peak positions could be determined with the accuracy of a single channel.

Counting losses due to mainly two factors must be corrected. (1) The resolving time of the system $69.8 \pm 2.4\ \mu s$ was measured with the source-pulser method and used for the correction of the losses. (2) Losses due to the setting of the discrimination level to cut noise signals was estimated to be $2.90 \pm 0.50\%$, by extrapolation of the low-pulse-height region to zero pulse height. In this estimated value, the loss due to the wall effect is included. The theoretically calculated loss was 3.2%, due to wall effect (2.72%) and low energy β-ray discrimination (0.48%). The radioactivity measurement with the PSPC method is as follows. The count rate, after subtracting the background count rate, in the region between the arrows in Fig. 2-26(d) corresponding to the peak positions in Fig. 2-26(e) is multiplied by the ratio 3.152 ± 0.006 of the total volume of the counter system including the pump to the volume (defined volume) between the arrows in Fig. 2-26(a), corresponding to the position calibration sources. The total radioactivity injected into the counter is obtained in this way. The radioactivity determined was 190.90 ± 1.52 Bq with the PSPC method and was 189.90 ± 2.05 Bq with the DLPC method. The ratio of the activity with the PSPC to that with the DLPC

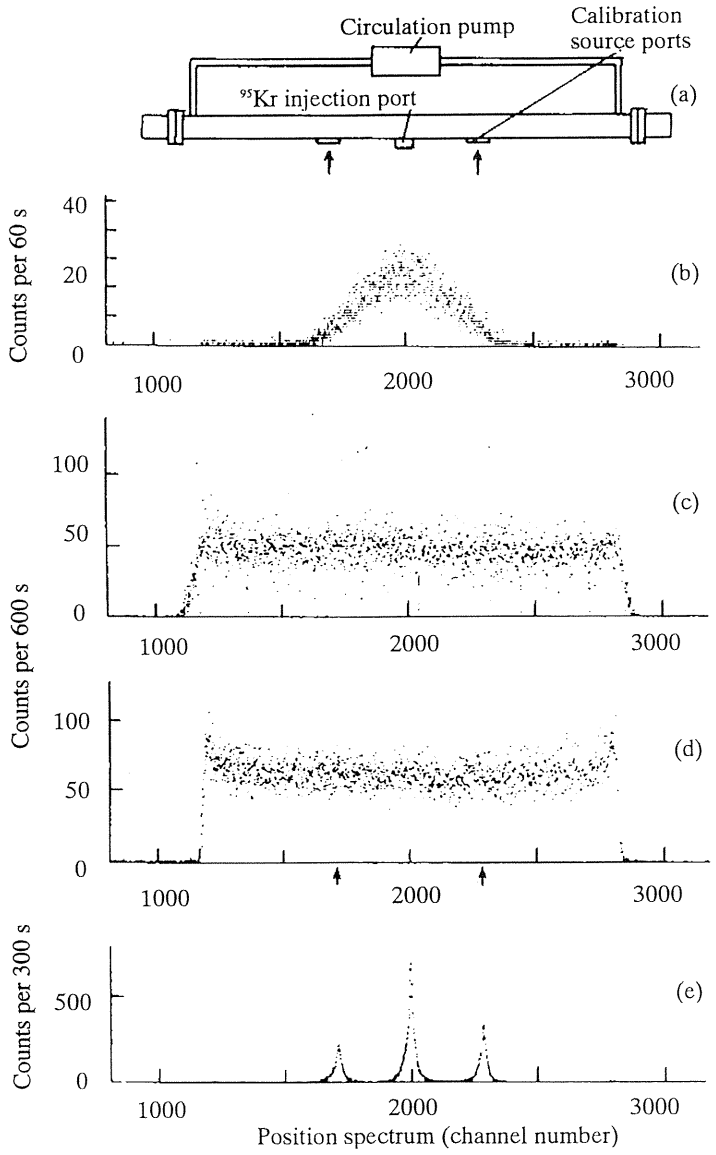

Fig. 2-26 (a) Position sensitive proportional counter, and position spectra (b) obtained just after injection of ^{85}Kr, (c) obtained with linear amplifier output after diffusion, (d) with logarithmic amplifier output, and (e) for position calibration sources.

was 1.005 ± 0.013 which showed very good agreement between the two. In estimating the error for the count rate in the PSPC method, the following factors were taken into account: statistical error 0.50%, the error due to the correction for pulses under the discrimination level 0.50%, defined volume error 0.27%, volume ratio error 0.19%, the error due to resolving-time correction 0.17%, and similarly in the DLPC method, statistical error 0.94%,

under discrimination correction error 0.50%, the error due to resolving-time error 0.17%. In the case of ^{85}Kr, the low intensity β-ray (0.415 MeV) with emission rate of 0.43% does not give any effect on the determination of radioactivity.

Diffusion in long proportional counter method developed for a method of routine radioactivity absolute measurement for ^{41}Ar[2-22] as well as ^{3}H, ^{14}C and ^{85}Kr[2-23,2-24,2-25].

2.3 Neutron position-sensitive proportional counter

In the field of nuclear reactor physics, they need the information on geometrical distribution of thermal and fast neutron fluxes. Gold wire activation method is usually used, which takes more than four or five hours and the position resolution is usually not less than 5 mm. We tried to develop neutron PSPC which were able to obtain real-time information on neutron distribution in reactor experiments.

2.3.1 He-3 neutron position-sensitive proportional counter

The PSPC with the double cathode tube described in the section 2.2.1.4 was used to measure neutron flux distributions in the Kyoto University Critical Assembly (KUCA). The experiment was done at the B core[2-26] of the KUCA shown in Fig. 2-27. The dimension of each grid was 5.53 cm × 5.53 cm square. The reactor power of the assembly was monitored with the uncompensated ionization chamber #5. The counter was inserted into a hole of 2.8 cm diameter in the polyethylene reflector at K-15 (marked with P).

Figure 2-28 shows the neutron flux distribution measured by means of the counter at K-15 and those measured by means of bare fine gold wires with a diameter of 0.5 mm at the cross point of lines K-15,16, and L-15,16 with and without the counter at K-15. They were

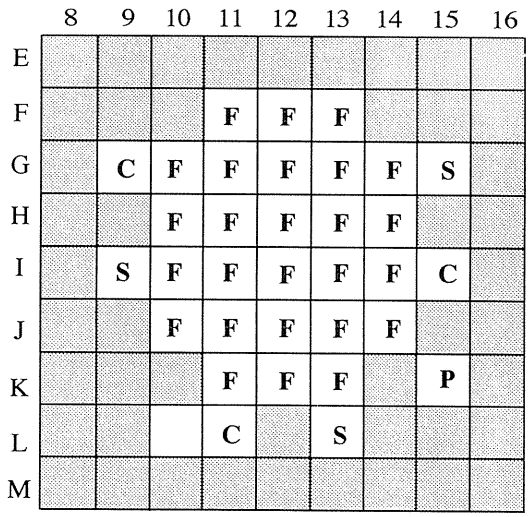

F:Fuel element **C**:Control rod
S:Safety rod Blank:Void
P:Position-sensitive proportional counter
Screened area: Polyethylene reflector

Fig. 2-27 Schematic top view of the core of KUCA.

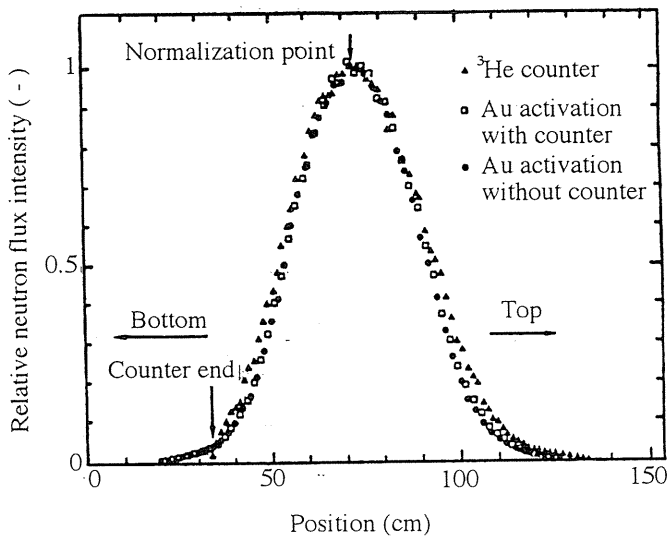

Fig. 2-28 Neutron flux distributions measured by means of counter (▲), Au wire activation method with counter (□), without counter (●).

normalized for comparison at the peak position of the measured distributions. It took only three minutes to obtain the distribution by means of the position-sensitive counter, although the reactor power of the KUCA for the measurement was about three orders of magnitude less than that for the measurements by means of gold wires. On the other hand it took about half a day to obtain the distribution with the gold wire activation method. The two distributions obtained with the gold wires, which were measured under the conditions with and without the counter, approximately agreed with each other.

On close investigation, however, there was slight difference between the above two distributions; at both tails in the bottom and the top regions of the distribution, the measured neutron flux with the counter was slightly higher than that without the counter. Similarly, the distribution measured by means of the counter was higher than the results obtained with gold wires at both tails. The difference for latter case can not be explained by the broadening of the distribution due to the position resolution of the counter mentioned later. Therefore it was considered that the differences were due to the streaming effect of thermal neutrons through the counter. Because the mean free path of thermal neutrons in the counter was 260 cm, the counter might simply work as a void. Therefore when the counter existed, neutron fluxes at the bottom and the top regions around the counter were presumably rather high due to the streaming effect. The existence of the neutron streaming effect through the counter insertion hole was confirmed by the measurement of neutron flux distribution with the position-sensitive counter laid horizontally on the top surface of the core assembly along the line J, where the empty insertion hole was moved to J-8. The strong neutron streaming was observed around the insertion hole. This result supported the above consideration that the neutron fluxes became high at the bottom and the top regions around the counter insertion hole due to the streaming effect of thermal neutrons.

2.3.2 Nuclear fission counter

As shown in Fig. 2-29, one end of a resistive anode rod with 50 kΩ resistance and 5 mm diameter is grounded for the signal current through a high voltage ceramic capacitor (2200 pF, 6 kV); the signal v_a is obtained from the other end. The inner surface of the cathode is coated with uranium oxide (natural uranium)[2-27,2-28]. The cathode is covered with a shielding tube. The cathode signal v_c is proportional to the total charge and the division v_a/v_c gives position information x/L[2-29], where x is the position of the detection of the fission fragment and L is the counter length.

The outer diameter and the effective length are 2.5 cm and 50 cm, respectively. The counting gas is P-10 gas with atmospheric pressure. Because two pre-amplifiers are located at one end of the counter, the counter can be inserted into a narrow space.

The inner surface of an unfolded aluminum foil with 80 μm thickness is coated with a mixture of fine UO_2 powder and electric conductive binder (Electrodag 181) with weight ratio 2:1. The average range R_f of fission fragments is about 15 μm in the coating. The count rate N_f of fission fragments per unit axial length of the counter is expressed by

$$N_f = 2\pi r n t \sigma_f \phi (1 - t/2R_f) \tag{2-21}$$

where is the radius of the foil cylinder, n is the number of uranium atoms per unit volume of the coating, t is the thickness of the coating, σ_f is nuclear fission cross section of natural uranium for thermal neutrons with flux density ϕ.

Since the total count rate must be in the range $1\text{-}10^4$ cps for practical use, the measurable neutron flux density ranges from 1×10^3 to 1×10^7 n/cm^2·s for the counter with r = 1 cm, the length L = 50 cm, n = 1.5×10^{21} atoms/cm^3 and t + 10 μm. For the measurement of intense neutron flux density up to 10^{10} n/cm^2·s, it will be necessary to decrease t to less than 0.1 μm with small uranium content and to make a strip coating with a width of less than 1 mm along an axial direction. It will be effective to exchange such a coated strip with appropriate uranium content depending on neutron flux density.

The total count rate $N_{T\alpha}$ of α-particles is expressed by

$$N_{T_a} = \pi r L n t \{\lambda_1 C_1 + \lambda_2 (1 - C_1)\}(1 - t/2R_\alpha)\,, \tag{2-22}$$

where λ_1 and λ_2 are α-decay constants of ^{235}U and ^{238}U, respectively, c_1 is the isotopic abundance of ^{235}U and the average range R_α of α-particles is about 22 μm in the coating. If

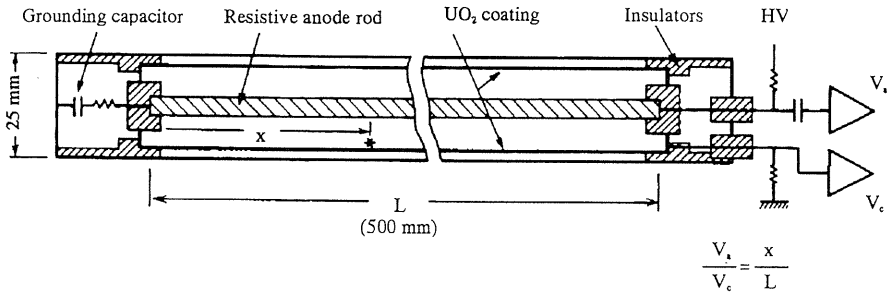

Fig. 2-29 Position sensitive nuclear fission counter.

$t \ll R$ or if t is known, we can determine the product nt from eq. (2-22) by using the total α-particle count rate $N_{T\alpha}$. Therefore, the neutron flux density can be determined from eq. (2-21) using nt and N_f.

Two kinds of uranium coating were adopted. One was a uniform coating throughout the inner surface of the aluminum foil cylinder for the measurement of the neutron flux density distribution. The other was a ring-shaped coating with varying width for the measurement of the position resolution.

The pulse height distribution from the fission counter is shown in Fig. 2-30. By referring the calculated pulse height spectra for 2π geometry[2-30], the UO_2 coating- thickness of our counter seems to be in the range $2.5 \sim 3\ \mu$m. It is not so difficult to distinguish between α-particle signals and fission-fragment signals. The position distribution measured with the counter of ring shaped coating with different width is shown in Fig. 2-31. Position resolution depended on the discrimination levels indicated by the arrows "lower" and "higher" in the pulse height distribution of Fig. 2-30. The true position resolution was 5 mm when all nuclear fission events were used to obtain the position distribution. The resolution will be improved, by increasing the gas pressure and choosing the gas kind.

There was no serious effect of ^{60}Co γ-ray irradiation with a dose rate of up to 10^3 R/h (0.3 C/kg · h) on α-particle spectrum. However, pulses with large pulse height comparable to those of fission fragments appeared at around 10^4 R/h.

2.3.3 Some applications

^{3}He neutron PSPC can be used under the combination of polyethylene neutron moderator for the flux, energy and incident direction of neutrons.

2.3.3.1 Energy detective long counter

A neutron counter that consists of a cylindrical moderator and a proportional tube inserted into the moderator is known as "long counter"[2-31]. With its flat detection efficiency over a wide range of neutron energy, it has been used as a standard neutron flux monitor. Various types of long counters have been developed to improve the flatness and increase the detection efficiency[2-32]. If we substitute a charge division type ^{3}He PSPC for an ordinary

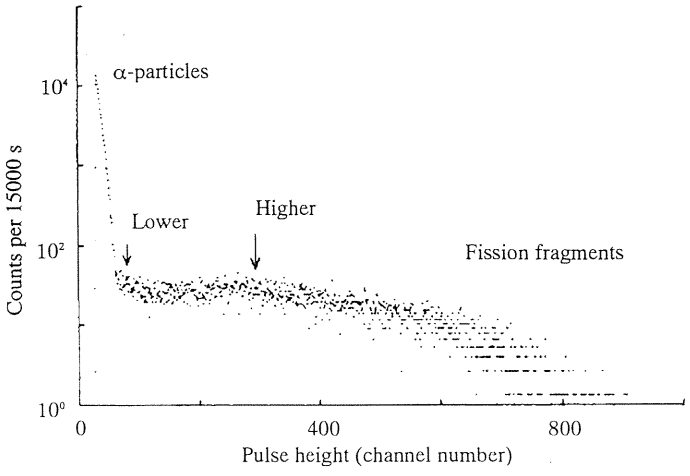

Fig. 2-30 Pulse height distribution from fission counter.

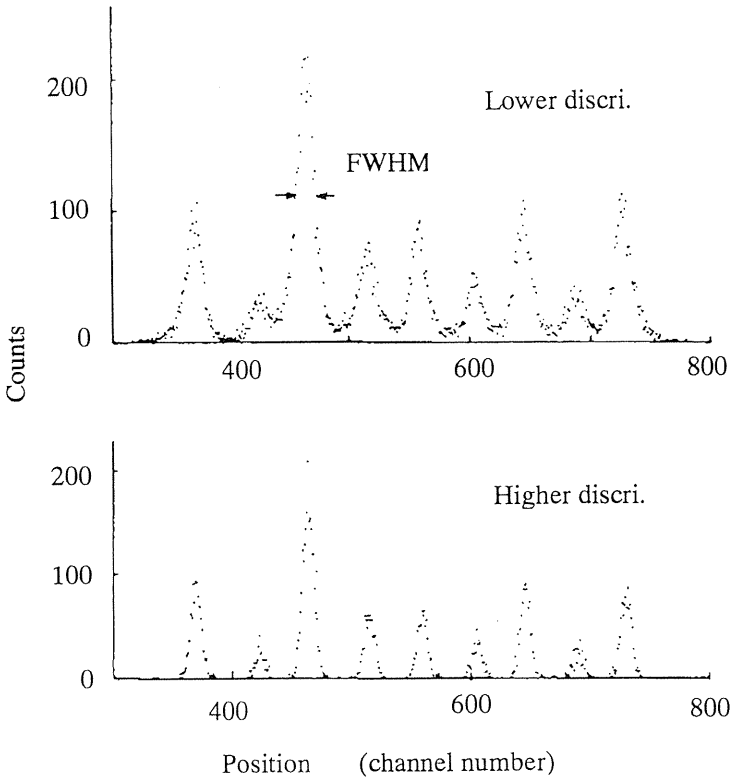

Fig. 2-31 Position spectra obtained with the counter for the measurement of position resolution with lower discrimination and higher discrimination.

proportional counter, a position profile of neutron detection that contains some information about neutron energy is obtained.

We, therefore, have developed a unique neutron counter as one of the applications of the PSPC to thermal-to-fast neutron measurement[2-33]. A schematic view of the Energy Detective Long Counter (EDLC) is shown in Fig. 2-32. Neutrons incident upon the front face of the EDLC lose their energy through collisions in the cylindrical moderator. Being thermalized, they are detected with a PSPC placed along the moderator axis. If the incident neutrons have sufficiently high energy, the mean free path is initially large and they undergo the first collision at an appreciable distance from the front face. After the first collision, the neutrons may undergo the second and the third collisions at a certain distance from the front face. Therefore, high energy neutrons can travel a considerable distance from the first collision point until they are thermalized and detected with the thermal neutron detector ^{3}He PSPC. This is not the case, however, for the relatively low energy neutrons. In that case, neutrons undergo the first collision near the front face of the EDLC, and, then, they are easily thermalized and detected with the PSPC. The mean detection positions for fast neutrons are therefore deeper than those for slow neutrons. In other words, the position profile of neutron detection may be applicable to a rough estimation of the incident neutron energy and, hence, neutron dose equivalent can be obtained.

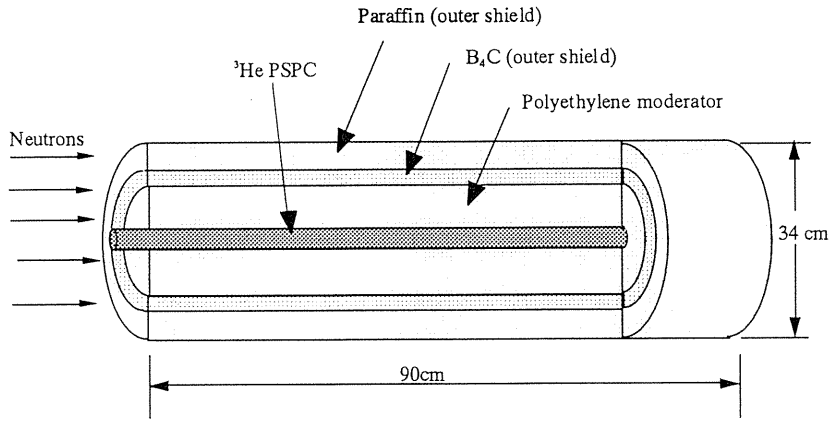

Fig. 2-32 A schematic view of the energy detective long counter (EDLC).

The EDLC shown in Fig. 2-32 consists of a PSPC with an outer diameter of 25 mm as a thermal neutron detector, a polyethylene moderator with a diameter of 16 cm and a length of 70 cm, and an outer shield made of B_4C and paraffin. The PSPC consists of coaxial double cylindrical tube and a resistive anode wire[2-29], so that signals are read from only the rear end of the counter. The counting gas is a mixture of ^{3}He (170 kPa) and CF_4 (30 kPa). The CF_4 gas decrease the ranges of proton and triton, and therefore improves the position resolution[2-10]. The counter has a position resolution of 1 cm and good integral linearity over the effective length.

A cadmium plate with a thickness of 2 mm was placed on the front face of the proportional counter to prevent direct incidence of low energy neutrons into the counter. The moderator was set in the outer shield to prevent room-scattered neutrons from entering the side of the EDLC, so that the EDLC is sensitive principally to neutrons incident onto the front face.

Neutrons with energies of 23 keV, 182 keV, 593 keV, 2.85 MeV and 5.0 MeV were incident nearly perpendicular to the front face of the EDLC. Neutrons with energy of 23 keV were produced by Sb-Be neutron source. Neutrons with energies of 182 keV and 593 keV were produced by the ^{7}Li(p, n)^{7}Be reaction with a Van de Graaff accelerator, while 2.85 MeV and 5.0 MeV neutrons were produced by the T(d, n)^{3}He and the D(d, n)^{3}He reaction with a Cockcroft-Walton and the Van de Graaff accelerators of Electrotechnical Laboratory[2-34], respectively. The distance between the targets and the front face of the EDLC was 2 meters. The position profiles were obtained for these neutrons energies, and also for thermal neutrons.

A Monte Carlo simulation code was developed to investigate the counter responses. It was based on the modification of the O5S code[2-35]. The cross section data were from the JENDL-3 nuclear data file[2-36]. The history of each of the neutrons incident on the counter was followed until the neutron escaped from the moderator or it interacted with a ^{3}He nucleus, producing a proton-triton pair from the ^{3}He(n, p)T reaction in the PSPCs. When the latter interaction took place, the interaction position in the PSPC was stored.

Figure 2-33 shows the experimental position profiles of neutron detection for various energies, normalized to the same integral counts. The front face of the EDLC corresponds to

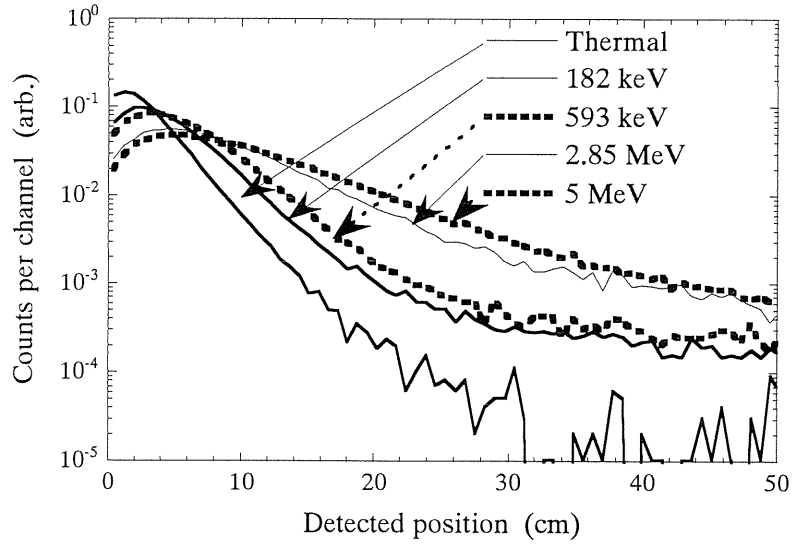

Fig. 2-33 Position profiles experimentally obtained for monoenergetic neutrons with the EDLC together with the simulation results shown with line.

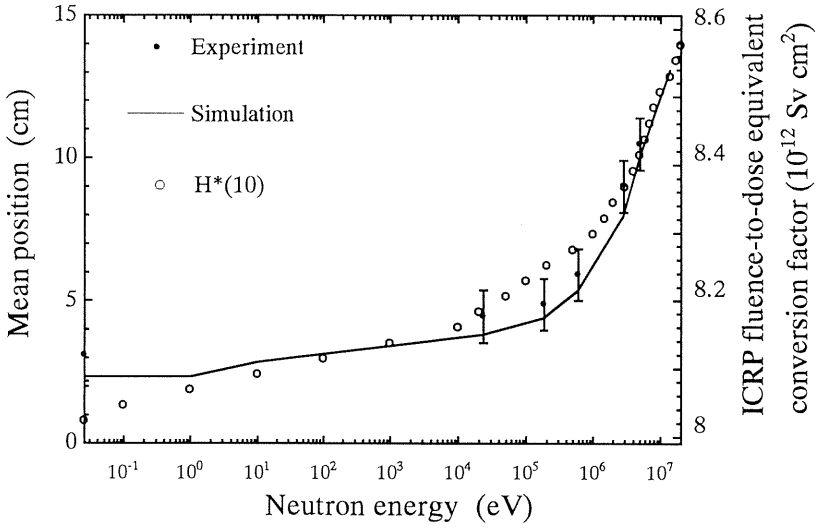

Fig. 2-34 Mean position of neutron detection (solid line) and ICRP fluence-to-dose equivalent conversion coefficient[2-47] (circles)

0 cm. Monte Carlo simulation results agreed with the experimental ones. The energy dependency of the position profile is clearly recognized.

A flat detection efficiency was obtained for the energy range from about 10 keV to 10 MeV. Figure 2-34 shows the mean detection position and ICRP fluence-to-dose equivalent conversion factor[2-37]. The mean detection position curve is similar to the dose equivalent

curve. Because the detection efficiency is almost flat, the dose equivalents can be roughly determined by calculating the mean detection position, even for multi-energetic neutron beams. Compared to a conventional spherical-type neutron dosimeter, this method has the advantage that information on the incident neutron energy and direction can be obtained.

2.3.3.2 Energy and direction detective spherical neutron counter

When neutrons are from many directions, a series of measurements by turning the EDLC for various directions should be necessary, because the EDLC gives only a one-dimensional position distribution of the neutrons thermalized in the moderator. We have developed another unique neutron counter that is sensitive to 4π direction. The method of extracting the energy information is similar to that of the EDLC. The present neutron counter is energy sensitive, hence, named as Energy Sensitive Spherical Neutron Counter (ESPHENEC)[2-38].

A schematic drawing of the ESPHENEC with the source-detector geometrical relation for Monte Carlo calculations is shown in Fig. 2-35. The diameter of the spherical moderator is 26 cm which was determined by the Monte Carlo simulations so that the counter had an extended response up to about 20 MeV. The outer and the inner diameter of the PSPC are 1 cm and 0.9 cm, respectively. The counting gas is a mixture of ^{3}He (101 kPa) and CF_4 (71 kPa). The PSPC has a good position resolution which was evaluated to be about 0.6 cm in FWHM when the applied voltage is 1500 V. The position of the neutron detection was calculated by the charge division method.

Four kinds of monoenergetic neutron beams, 165 keV, 3.0 MeV, 5.0 MeV and 14.9 MeV were generated by the Van de Graaff accelerator and the Cockcroft-Walton accelerator at

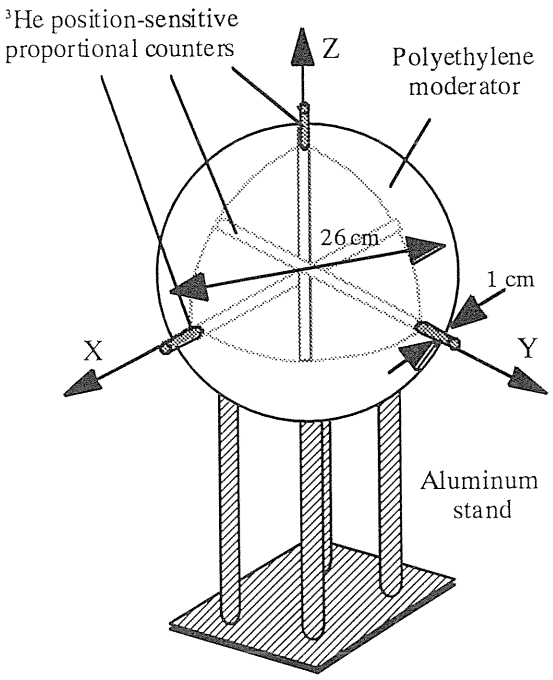

Fig. 2-35 A schematic drawing of the counter and the source-detector geometry.

Electrotechnical Laboratory. The neutron beams were incident on the ESPHENEC from three directions: (1.00, 0.00, 0.00), (0.85, 0.50, 0.00) and (0.71, 0.71, 0.00), that is 0°, 30° and 45° from the x-axis, respectively, with turning the ESPHENEC around.

Figures 2-36 (a) and (b) show the detection position profiles experimentally obtained for the beams of 165 keV neutrons incident from (1.00, 0.00, 0.00) and (0.71, 0.71, 0.00), respectively. Calculated position profiles, corresponding to the experimental ones, are shown in Figs. 2-36 (c) and (d). We found from the figures that the position profiles were sensitive to the incident direction of neutrons.

Because it is useful to obtain an information about the incident directions of neutron beams, we tried to estimate mean directions with the three position profiles obtained for the x-, the y-, and the z-PSPCs. To estimate the mean direction, we used a vector whose elements were the mean positions obtained with the three PSPCs. It is considered that the norm of the vector, or the distance from the origin to the point specified with the mean positions in the coordinate system, is important for the rough estimation of the neutron energy. However, it is easier to obtain the directional information on the neutron fluence independently of the neutron energy. Then, the directional information on the neutron fluence was shown with the direction cosine that indicated the mean direction of the incident neutrons. The direction cosine is conveniently called the CGA (Center of Gravity of the Angular distributions) vector. The experimentally obtained vectors and the calculated (with Monte Carlo simulation) ones agreed with the direction cosines that indicated real directions from which the neutron beams were incident.

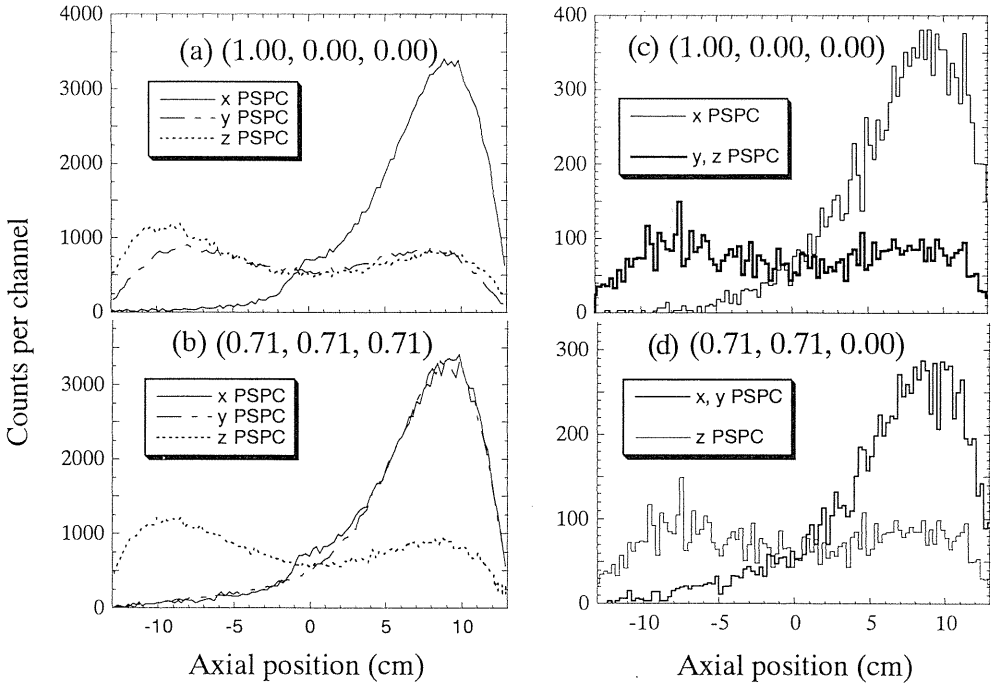

Fig. 2-36 Experimentally obtained detection position profiles for the 165 keV neutron beams from (a) (1.00, 0.00, 0.00) and (b) (0.71, 0.71, 0.00) are shown together with the simulated results (c), (d), which correspond to the experimental ones.

The sensitivity of the neutron counter in the *inner region* of the sphere is high for fast neutrons. On the contrary, the sensitivity of the *outer region* is high for slow neutrons. With increasing energy of the incident neutrons, the fraction of neutron detection around the central region (typically about −3 cm to 3 cm from the counter) increased.

When a point source was placed along the x-axis, the x-profiles showed strong energy dependency. On the other hand, the y- and the z-profiles did not significantly vary for a change of the initial energy of the incident neutrons. It can be seen that the profiles had a directional feature that should be suppressed to measure all the neutrons incoming from 4π directions as uniformly as possible. To reduce the directional dependency of the response functions, the x-, the y- and the z-profiles as functions of the radial position were added together

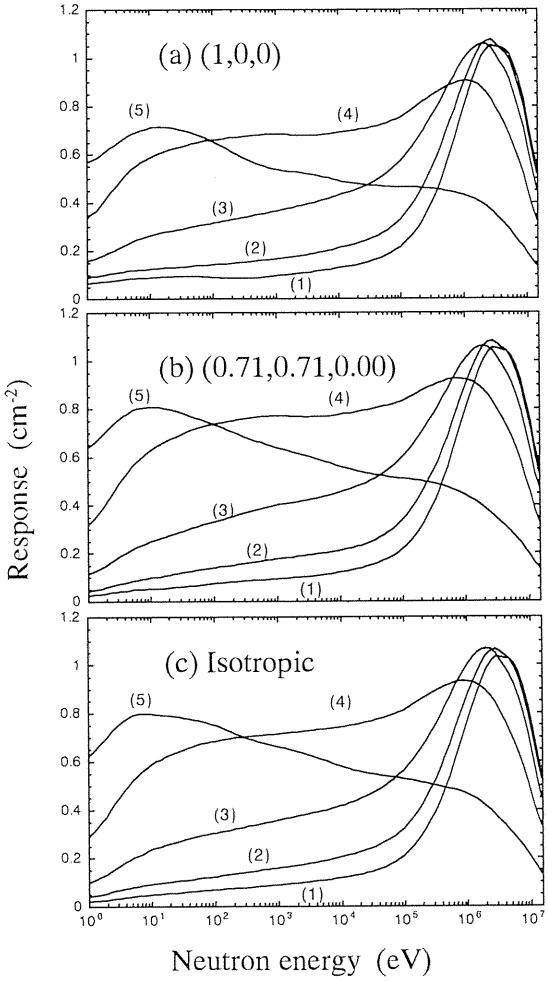

Fig. 2-37 Response functions of the counter calculated from the x-, the y- and the z-profiles by radially dividing the detection positions into five regions (1) ~ (5) (see the text) for different incident directions.

making the xyz-radial position profile. The curves shown in Fig. 2-37 (a) are the radially-divided responses as a function of the energy of the incident neutrons calculated for the point source geometry. The numbers in the figures indicate the radial regions of the spherical moderator: (1) 0 cm to 2.6 cm, (2) 2.6 cm to 5.2 cm, (3) 5.2 cm to 7.8 cm, (4) 7.8 cm to 10.4 cm, and (5) 10.4 cm to 13 cm. Each of the curves shows accumulated detection counts within one of the five radial regions normalized to the unit fluence. Figures 2-37 (b) shows the response function for the point source geometry in which the direction cosines that indicated the source location was (0.71, 0.71, 0.00). The source distance was 2 m for each of the fields. Figure 2-37 (c) shows the response functions for the isotropic field.

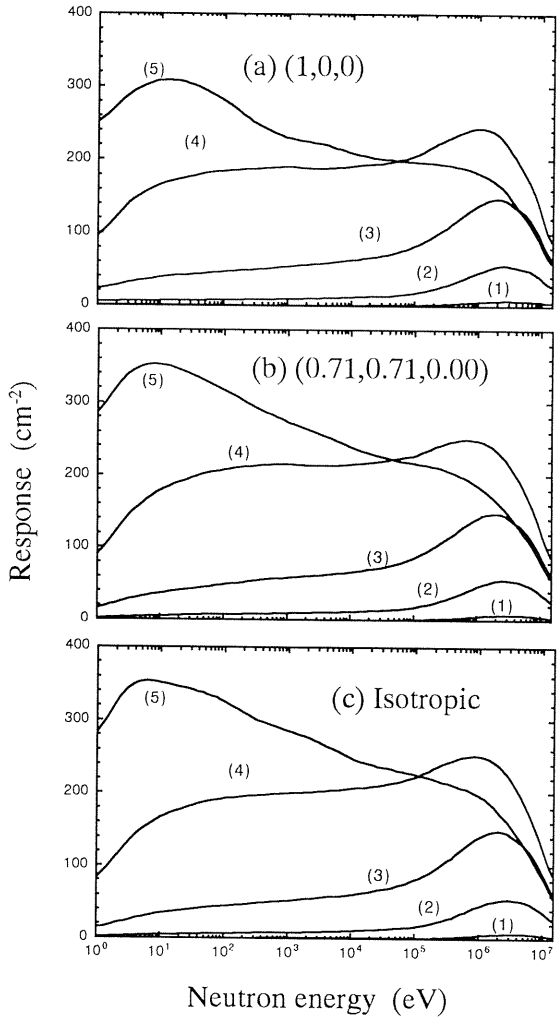

Fig. 2-38 Volume-weighted response functions calculated from the x-, the y- and the z-profiles by radially dividing the detection positions into the five regions. The numbers (1) ~ (5) indicate the same radial regions as those shown in Fig. 2-37.

Because the curves (1), (2) and (3) at the energy range higher than about 1 MeV are nearly identical, the response functions were not useful for spectrum measurements of high energy neutrons. Most of the energy spectra measured with the response functions were not acceptable as solution spectra. It is interesting, however, that the response curves are identical in these shell regions, because the feature indicated that the neutrons were fairly thermalized in these regions and their movements were random. The initial information on the direction of the incident neutrons is completely lost in the central shell region.

Another response functions were obtained with multiplying the counts within each shell region by the volume of the spherical shell. Figures 2-38 (a)–(c) show the "volume-weighted" response functions calculated for the same radial regions as that of the radially-divided response functions shown in Figs. 2-37 normalized to the unit fluence. Approximate

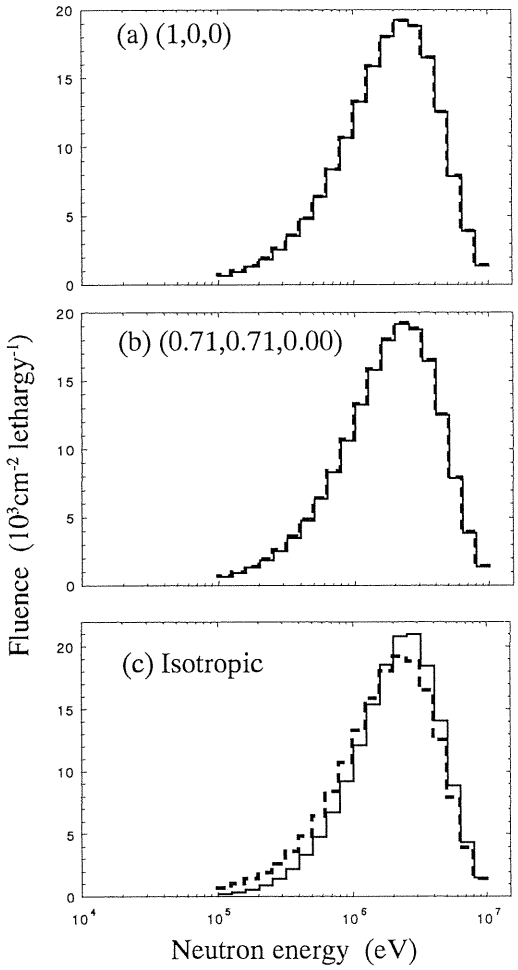

Fig. 2-39 Measured fluence spectra of neutrons from the spontaneous fission of ^{252}Cf unfolded with the volume-weighted response functions for different incident directions (a), (b), (c) of neutrons.

numbers of the thermalized neutrons that existed in the spherical shells, which are nearly independent of the incident directions, are estimated.

An experimental test of the counter using a ^{252}Cf neutron source was done at the standard neutron field of the Japan Atomic Energy Research Institute (JAERI). Spectrum measurements were done using each of the five sets of the response functions shown in Figs. 2-38 (a)—(c) for the experimental data measured for the direction cosine of (1, 0, 0). The energy range of the measured spectra was from 100 keV to 10 MeV where the directional feature of the response functions was not so significant. The unfolding code used here was the SAND-II[2-39]. Figures 2-39 show the fluence spectra of the neutrons from the spontaneous fission of the ^{252}Cf, unfolded with the volume-weighted response functions. The solid and the dashed line indicate the measured and the fission neutron spectrum of ^{252}Cf, respectively.

The response functions calculated for various fields were applied to the spectrum unfolding of the same experimental data. The spectra were shown in Figs. 2-39 (a)—(c). Most of the spectra except that of Fig. 2-39 (c) agree with the expected spectrum in spite of the different geometry of the response functions. On the other hand, Fig. 2-39 (c) shows a spectrum the shape of which is shifted to higher energy than expected when the isotropic response functions are used for the unfolding process. This is due to the directional feature of the response functions.

If there was no information on the source geometry, the spectrum measurement should be done with the isotropic response functions. One of the methods to gain information on the source location is to estimate a mean direction by calculating the center of gravity of the axial positions for each position profile[2-38]. In the experiment done at the JAERI field using the ^{252}Cf neutron source, the centers of gravities of the x-, the y- and the z-profiles were 4.66 cm, −0.33 cm and 0.28 cm, respectively, and, hence, the mean direction was calculated as (0.996, −0.071, 0.060), which is close to the original value of (1, 0, 0). We can find from the CGA vector that the response functions for (1, 0, 0) are most suitable for the spectrum measurement in this case.

The estimation of the mean direction was only useful in a single-point source geometry under no significant influence of room-scattered neutrons. Even when the proper direction of the neutron source could not be deduced, however, spectrum measurements were possible in the energy range from 100 keV to 10 MeV because the directional feature of the response functions was not so significant. It is necessary to further improve the response functions to give the best energy resolution.

III. Optical Fiber Position Detection Method

Optical fibers are now widely used for light transmission in various fields. In the field of radiation measurement, they are used for light transmission and also scintillation fibers are used.

We newly developed optical fiber method[3-1,3-2,3-3] in which the tip of an optical fiber was painted with mixture of ZnS(Ag) scintillator, neutron converter and adhesive material, and the fiber was automatically moved.

3.1 Neutron distribution detection

Scintillation powder ZnS(Ag) and neutron converter LiF of natural lithium were mixed with adhesive paste and painted with a thickness of about 0.3 ~ 0.5 mm on the tip of plastic fiber with a diameter of 2 mm as shown in Fig. 3-1.

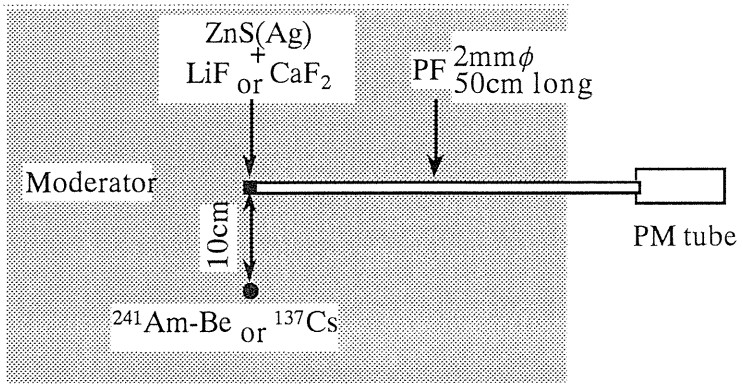

Fig. 3-1 An optical fiber neutron detector whose tip was painted with a mixture of neutron converter and scintillator.

The new simple detector with an outer diameter of 2.5 mm was tried to apply to the neutron flux distribution measurement in the core of Kyoto University Critical Assembly shown in Fig. 2-27. The point which is different from the fuel element in Fig. 2-27 is that; among many elements, 25 elements contain fuel part and each is consisted of fuel part at the center with a length of 37.6 cm, aluminum spectrum shifter (this is different point) at the upper part with a length of 20.3 cm and polyethylene moderator at the lower part with a length of 56.6 cm. Other elements are consisted of only polyethylene moderator through the whole length. At the position K-14 in the Fig. 2-27, of polyethylene moderator has vertical two holes with a diameter of 10 mm at the center (hole A) and at the corner (hole B, near the fuel elements) to be inserted the detector into them. In the experiments, the fiber was inserted beforehand deep into a hole and then pulled it up under automatical control with a computer.

Figure 3-2 (a) shows the results obtained in the measurement time of only 10 minutes. In the hole A, there is a polyethylene moderator with a thickness of 20 mm between the hole and the nearest fuel element, which moderates neutrons and the distribution detected by ^{6}Li(n, α)T reaction, in this case ^{6}Li enriched to 95% was used, shows the thermal neutron distribution. On the other hand, in the hole B, since there is no moderator between the hole and nearest fuel element, neutrons from the fuel element are not fully moderated and the count rates at the middle part are not so large compared with those in the hole A. At the lower part where there are polyethylene moderators in all fuel elements and therefore large count rates are obtained.

Figure 3-2 (b) shows the distributions obtained with gold wire activation method corrected by cadmium sheath method, which took $(4 \sim 5) \times 2$ hours to obtaine the results exhibiting rather large statistical errors due to the small count rates compared with the fiber method. Also the position resolution is only 10 mm due to the cutting interval of the activated gold wire, whereas the fiber method has the position resolution of about 1 mm as shown later in Fig. 3-3 (c).

Figure 3-3 (a) shows the configuration of each fuel element which is consisted of various cell components and each cell is consisted of uranium part and polyethylene part. Figure 3-3 (b) shows the distribution of thermal neutrons obtained by the fiber method (open circles) for 20 minutes measurement by inserting the fiber detector into the very narrow space between the fuel elements and the distribution obtained by gold wire activation method for $(4 \sim 5) \times 2$

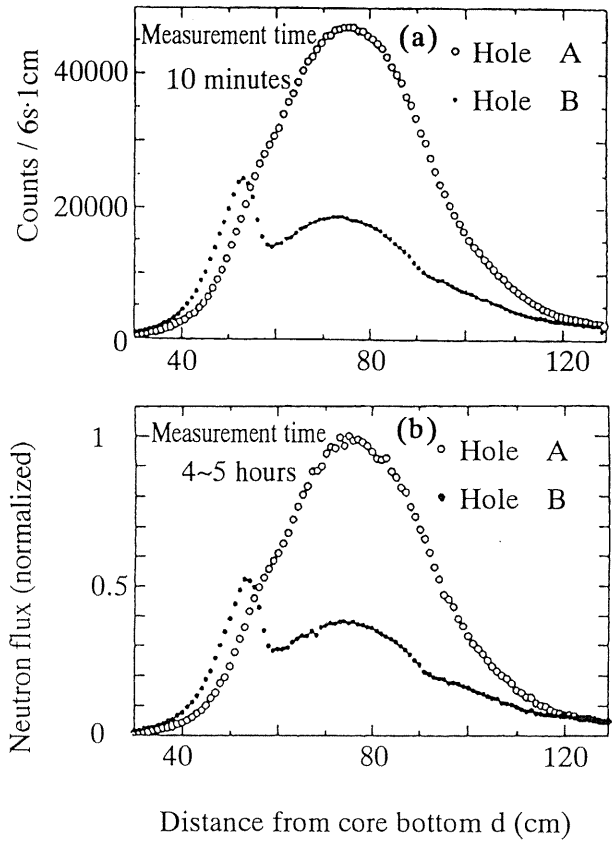

Fig. 3-2 Thermal neutron flux distribution obtained by optical fiber detector with natural lithium converter (a), and the distribution obtained by conventional gold wire activation method (b).

hours. The both are similar, but not the same due to the difference of the neutron energy dependence of the cross sections for both nuclear reactions. Figure 3-3 (c) shows the distribution of the enlarged portion from 67 cm to 94 cm in the part of (b). As is shown the fine structure of the distribution can be revealed.

When nuclear fission reaction can be used, the pulse height would be very large compared with ^{6}Li reaction and recoil proton reaction, so that the discrimination between pulses from such reactions or γ-ray interactions and those from fission reactions will be more easy and clear. Figure 3-4 shows the distribution obtained with enriched ^{6}Li converter, open circles, and that obtained with ^{235}U converter enriched to 16%. The sensitivity in ^{235}U method is more than 2 decades smaller than ^{6}Li method, which means ^{235}U method will be useful in the intense field of thermal neutrons.

Thorium-232 has nuclear fission reaction cross section only for fast neutrons with the energy more than about 1.1 MeV and the natural abundance of the nucleus is fortunately 100%. We tried to use this converter for the measurement of fast neutron distribution in the fast neutron source reactor "Yayoi" of The University of Tokyo. Figure 3-5 shows pulse

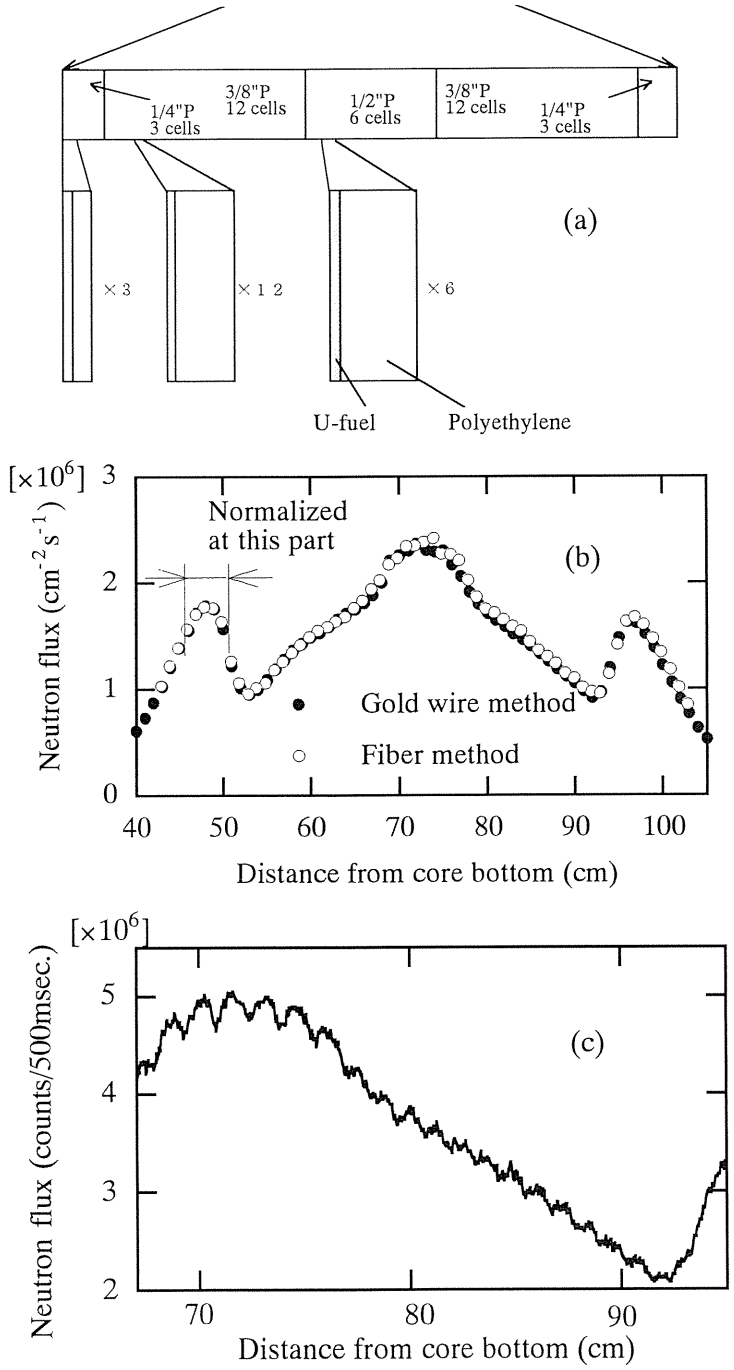

Fig. 3-3 A fuel element structure of KUCA and an expanded views of the parts (a), thermal neutron flux distribution obtained with fiber method compared with gold wire method (b) and the fine structure (c) of the distribution in a part of (b).

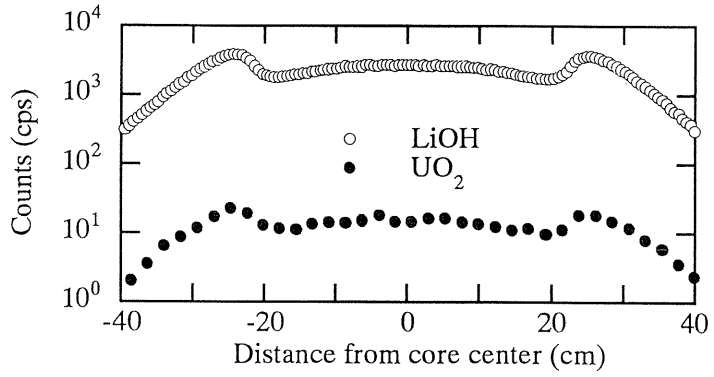

Fig. 3-4 Thermal neutron flux distributions obtained with ^{6}Li converter and ^{235}U converter.

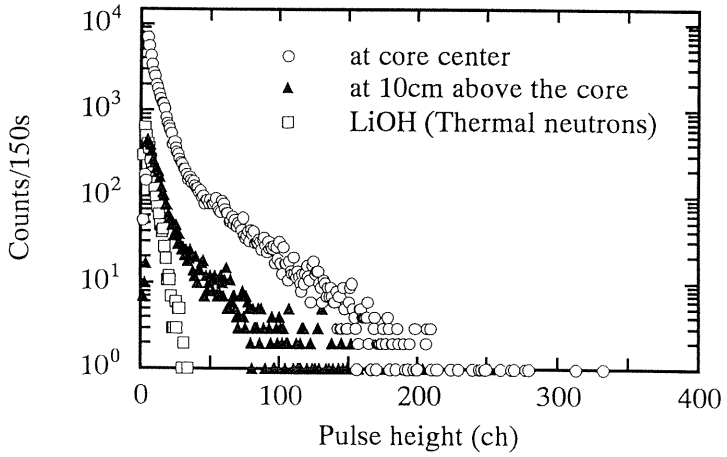

Fig. 3-5 Pulse height distributions in the fast neutron source reactor "Yayoi" obtained with ^{232}Th converter and ^{6}Li converter.

height distributions in the reactor. The distributions at the core center (circles) and at 10 cm above the core center have large pulse heights compared with those obtained with ^{6}Li detector. The pulse height due to γ-rays is far smaller and only the fission reaction can be observed. Figure 3-6 shows fast neutron distribution obtained by ^{232}Th converter.

3.2 γ-ray distribution detection

For γ-ray detection, it is necessary to eliminate neutron converter ^{6}Li, ^{235}U or ^{232}Th and adhesive material consisted of organic material which emits recoil protons by fast neutrons. By the same reason, plastic fiber is not suitable.

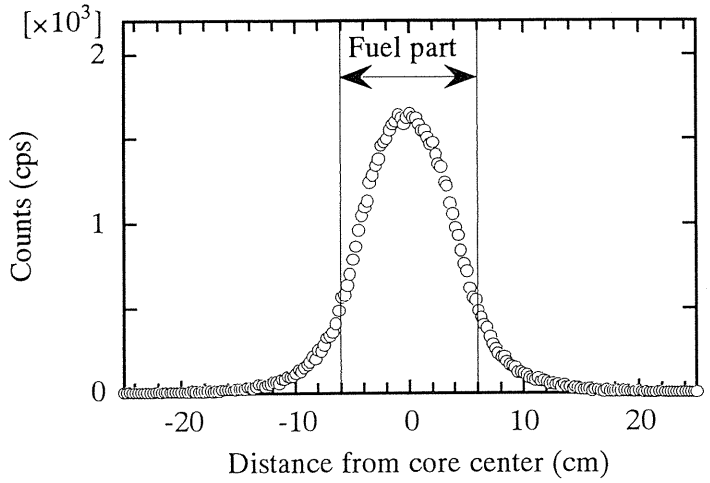

Fig. 3-6 Fast neutron flux distribution in "Yayoi" reactor obtained with ^{232}Th converter.

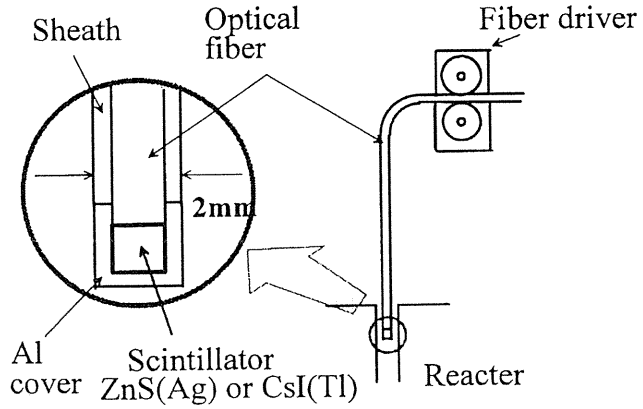

Fig. 3-7 Structure of scintillator part for γ-ray detection.

We designed γ-ray detector part as shown in Fig. 3-7. Scintillation powder of ZnS(Ag) is enclosed in an aluminum cap with a thickness of ~0.15 mm on the tip of a quartz fiber with a diameter of 0.7 mm. For the comparison, adhesive material and plastic fiber were used.

Nuclear activation of the component elements irradiated with 1.0×10^8 n/cm^{2}s for 1 hour in Kyoto University Critical Assembly (KUCA) showed no significant effect.

Figure 3-8 shows pulse height distributions obtained with ZnS(Ag) scintillator on the tip of plastic fiber. To find the effect of Cerenkov light, only a plastic fiber was irradiated with ^{137}Cs γ-rays. Pulses larger than electronic noise pulse can be seen. When ZnS(Ag) scintillator was attached, pulses larger than Cerenkov light are seen. Under the irradiation of ^{241}Am-Be neutrons and γ-rays, γ-pulses are surely observed compared with ^{137}Cs γ-rays. Pulses with

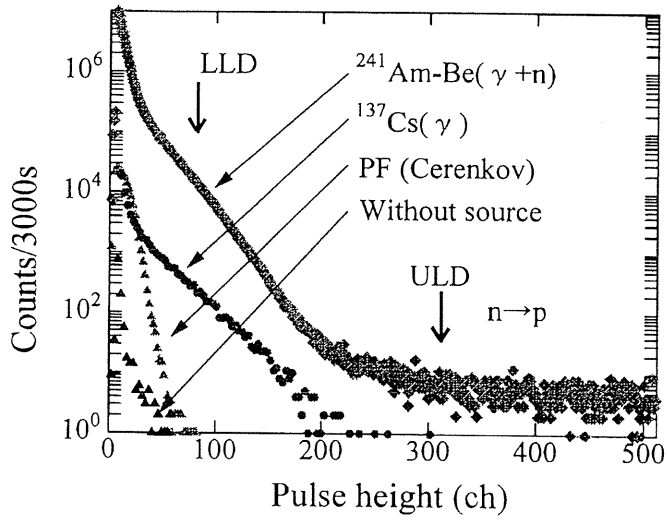

Fig. 3-8 Pulse height distributions obtained without source (▲), plastic fiber with source (▲), fiber with ^{137}Cs γ-rays (●), fiber with ^{241}Am-Be source (◆). LLD and ULD show lower and upper levels of a single channel pulse height analyzer.

much larger pulse height are seen, which are able to substantially discriminate by using a single channel pulse height selector (SCPHS) and by subtracting the part of recoil proton from plastic fiber under the extrapolating the much larger pulse height part.

Figure 3-9(a) shows γ-ray flux distribution in KUCA which was obtained by choosing pulse height with SCPHS (LLD, ULD) as shown in Fig. 3-8. By selecting pulses much larger than higher level discrimination, fast neutron distribution in Fig. 3-9(b) can be obtained due to the effect of recoil proton. For comparison, thermal neutron distribution was measured by using ^{6}Li converter as shown in Fig. 3-9(c). Differences between distributions of γ-rays, fast neutrons and thermal neutrons are seen.

When CsI(Tl) scintillator is used, different position profile is obtained. Figure 3-10(a) shows mass absorption coefficients of CsI(Tl) scintillator and ZnS(Ag). CsI has large absorption coefficient at around several hundred keV and more transparent for the scintillation light than ZnS(Ag), so that pulse height distribution contains large pulses and large count rate as shown in Fig. 3-10(b).

Figure 3-11(a) shows position distribution profiles obtained in KUCA. Large count rate was obtained with CsI scintillator. When we normalize CsI distribution to ZnS one at the both slopes, large count rate is obtained with CsI at the central fuel part. This phenomenon is more clearly seen in Fig. 3-11(b) obtained in fast neutron source reactor "Yayoi". The fuel element has large atomic number materials at the both sides of fuel part, which implies that at the fuel part rather low energy γ-rays, which are efficiently detected by CsI detector, are emitted from the fuel part, whereas at the both slope parts low energy γ-rays are absorbed by blanket parts and reflection parts, and therefore γ-ray energy distributions become hard, where absorption coefficients of both detectors are same. By using fiber detectors with different atomic number scintillators, it is possible to have the information about γ-ray energy distributions.

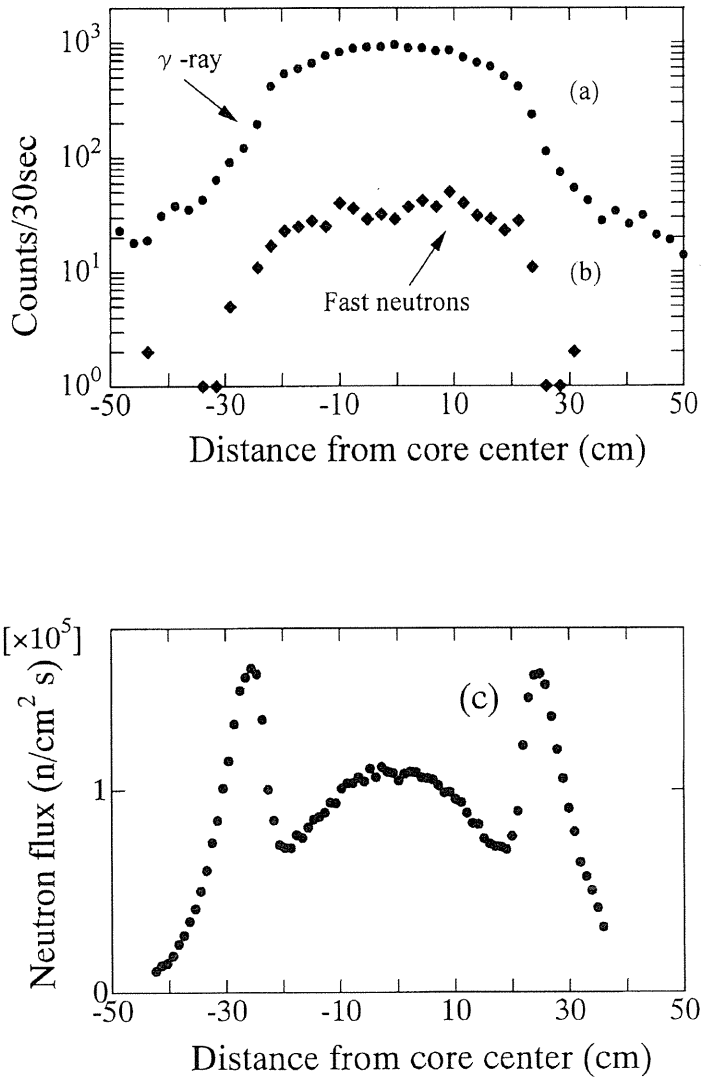

Fig. 3-9 γ-ray position distribution (a), fast neutron distribution (b), and thermal neutron distribution (c).

IV. Imaging Plate Method

Imaging Plate (IP) has a very high sensitivity of approximately $10^{2\sim3}$ times to that of conventional X-ray films, high position resolution of 100 μm × 100 μm, large dynamic range up to 10^5, and a large area up to 35 cm × 43 cm[4-1,4-2].

We investigated some characteristics of IP and applied IP to the distribution measurements of natural radioactivities in stone or in vegetables. We also proposed the identification method of the kinds of incident radiations.

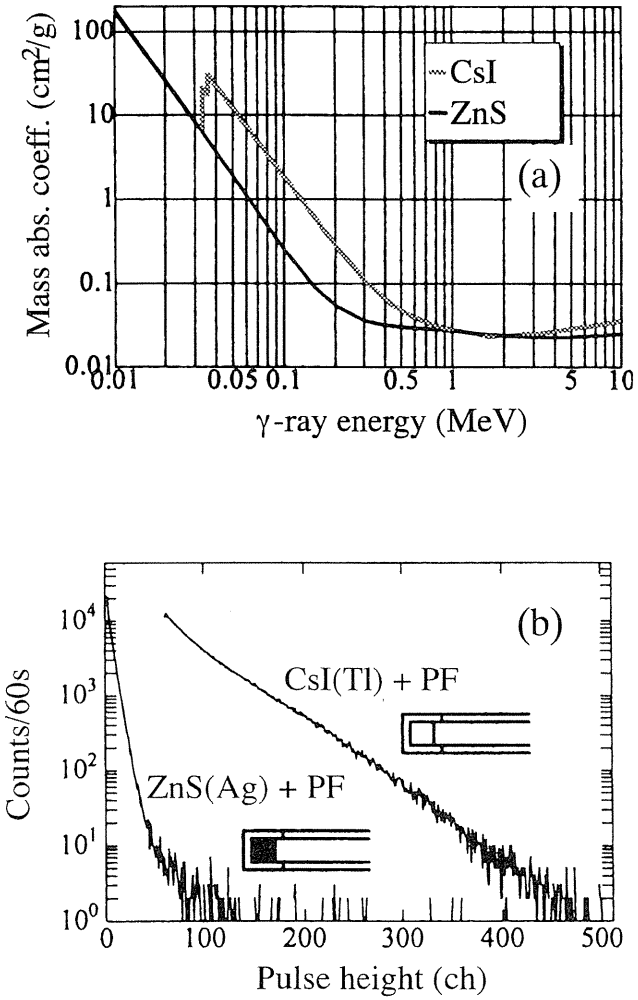

Fig. 3-10 Mass absorption coefficient vs. γ-ray energy (a), and pulse height distribution (b) with ZnS(Ag)-fiber and CsI(Tl)- fiber.

4.1 Fundamental Characteristics

4.1.1 Fading of the latent image

The latent image produced by radiation exposure fades with time after exposure[4-3,4-4] as shown in Fig. 4-1 for the image produced by ^{137}Cs γ-rays. In the reading instrument of PSL, the output is expressed by its own light intensity unit "PSL" defined in the IP system. Therefore, $(PSL)_0$ in the figure is the PSL intensity readout just after exposure for 5 min in our experiment and $(PSL)_t$ is the PSL intensity readout after t min of the same 5 min exposure. The fading depends on the atmospheric temperature.

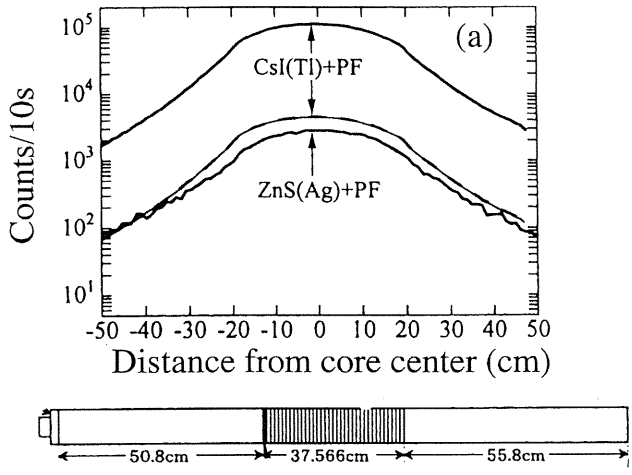

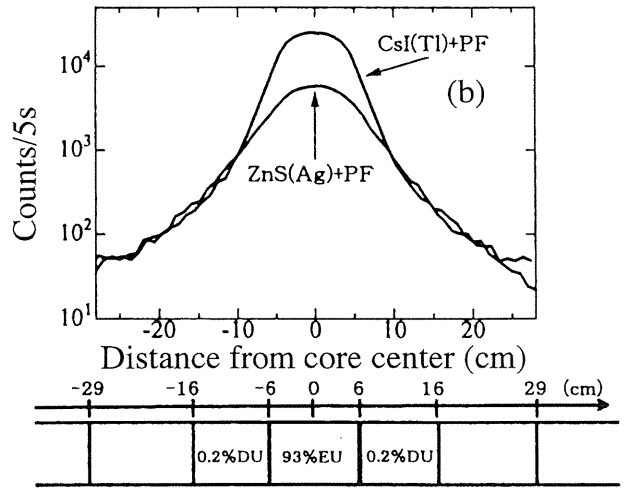

Fig. 3-11 γ-ray position distributions in KUCA (a), and those in "Yayoi" reactor (b).

The fading curve at 20°C is expressed simply by the following equation;

$$(PSL)_t/(\mathrm{PSL})_0 \equiv Y(t)$$
$$= 0.18\exp\left(-\frac{t}{8}\ln 2\right) + 0.31\exp\left(-\frac{t}{250}\ln 2\right)$$
$$+ 0.51\exp\left(-\frac{t}{7\times 10^5}\ln 2\right) \qquad (4\text{-}1)$$

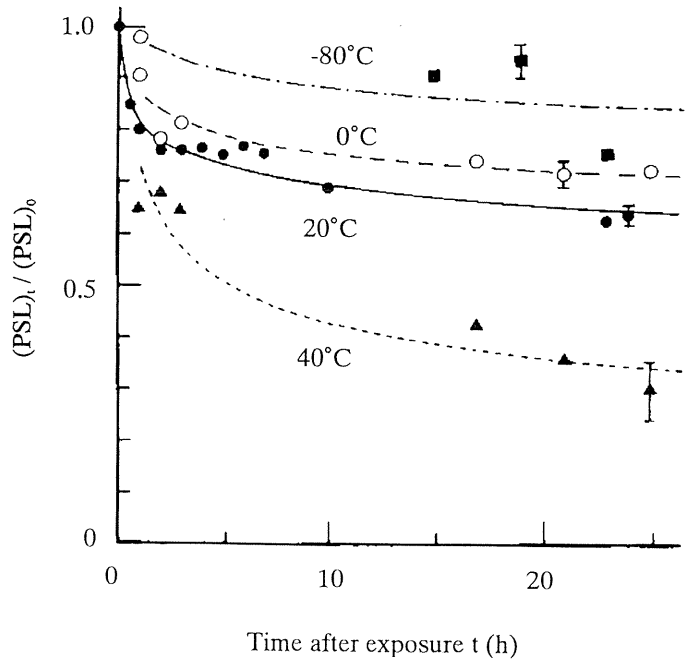

Fig. 4-1 Fading of latent image produced by ^{137}Cs source, at different atmospheric temperatures, shown as relative value of $(PSL)_t$ intensity to $(PSL)_0$ intensity just after exposure.

When the exposure is carried out for a rather long period of T min for a certain radioactive source or for back ground, the ratio of $(PSL)_T$ intensity obtained just after the exposure to $(PSL)_0$ is given by the following equation using Eq. 4-1

$$(PSL)_T/(PSL)_0 = \int_0^T Y(t)dt \tag{4-2}$$

4.1.2 The ratio of laten image intensity to prompt luminescence intensity

Imagine Plate emits prompt luminescence (PL) when a radiation enters. The ratio of PSL intensity from latent image to prompt luminescence intensity depends on the type and energy of incident radiations[4-5]. The ratio is smaller for the radiation with larger stopping power such as α-particle.

In the experimental procedure, when radiation entered IP, each PL intensity and the number of incident radiations were measured with a photomultiplier. Immediately after that, IP was irradiated with He-Ne laser beam 10 times and the total PSL intensity was measured by summing the PSL intensity of each reading. Then the ratio of PSL intensity to PL intensity per an incident particle was obtained. The ratio is shown in Fig. 4-2 as a function of the stopping power of the incident radiations. It decreases with increasing the stopping power. Because the ratio for oxygen ion is 0.51, about 66% (1/(0.51 + 1)) of excited electrons, effective to emit photons, from valence band are spent to emit PL and 34% of them are

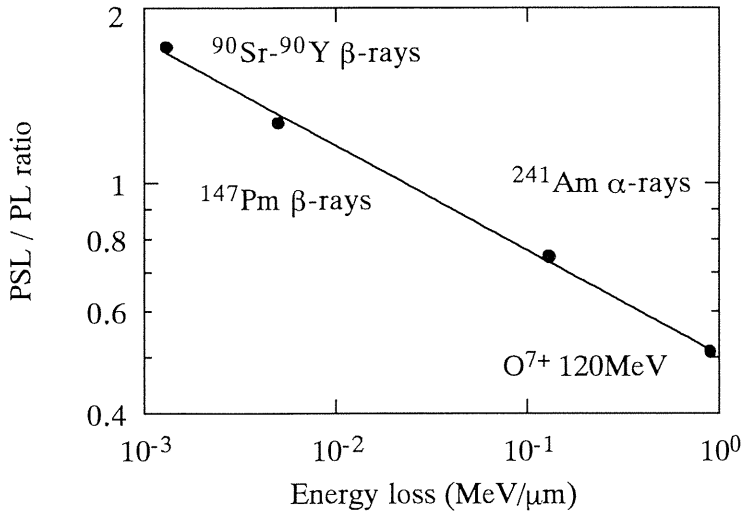

Fig. 4-2 The ratio of PSL intensity to PL intensity versus. energy loss of incident radiations.

trapped by F-center as latent image. When a β-particle from ^{90}Sr-^{90}Y enters on the other hand, about 37% of excited effective electrons are spent to emit PL and 63% of them are trapped by F-center.

An electron excited by an incident particle has a probability that it recombines with trapped holes and emits PL and a probability that it is trapped by an F^+-center and becomes F-center. The probability of the emission will depend on the densities of trapped holes and residual F^+-centers. If holes distribute densely and F^+-centers thinly caused by a high-stopping-power particle incidence such as α-particle, the probability of emission will be large. Therefore, the ratio of PSL intensity to PL intensity is small. On the other hand, if holes distribute thinly and F^+-centers densely caused by a low-stopping-power particle incidence such as high energy β-particle, the probability to emit luminescence will be small and many electrons would be trapped by F^+-centers. Then the ratio of PSL intensity to PL intensity is large.

4.2 Application for natural radioactivity distribution

4.2.1 Reduction of background radiations with shielding box

The inner surface of a lead shielding box seems to be emitting β-rays from ^{210}Bi or photoelectrons excited by X(γ)-rays[4-6,4-7]. PSL intensity per $mm^2 \cdot$ min abruptly decreased in a thickness of 0.2 g/cm^2 of lining material of Lucite or aluminum on the inner surface of the shielding box. The thickness of 0.2 g/cm^2 corresponds to about 500 keV electron range. γ- and X-rays were slightly absorbed by additional successive graded shield of Cd, and Cu. Additional lining plate of Cd seemed to emit more photoelectrons than Cu, therefore Cd additional lining slightly increased PSL intensity.

Summary results of shielding are shown in Fig. 4-3. In the figure, Pb 10 cm, Cd 1 mm, Cu 1 mm, Lucite 10 mm which means Pb 10 cm shielding box whose inner surface is successively lined with Cd, Cu and Lucite as mentioned above, is very good graded shielding for IP.

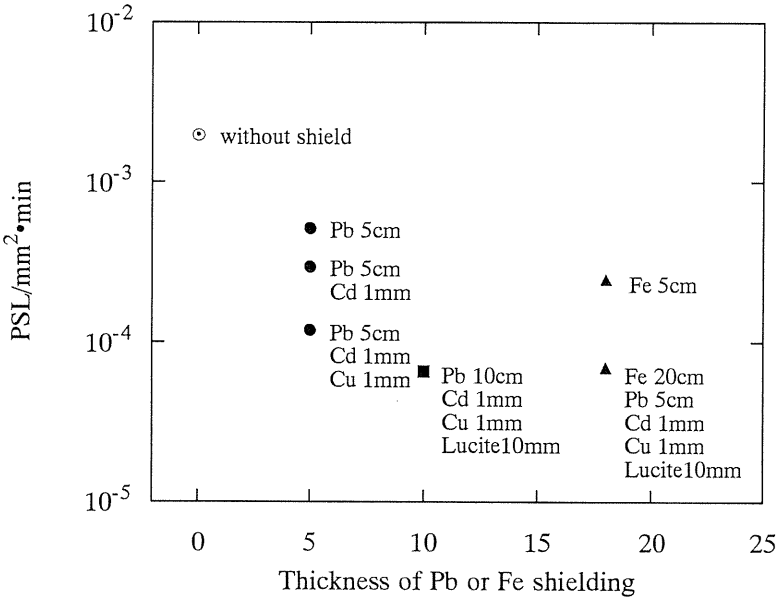

Fig. 4-3 Effect of graded shielding.

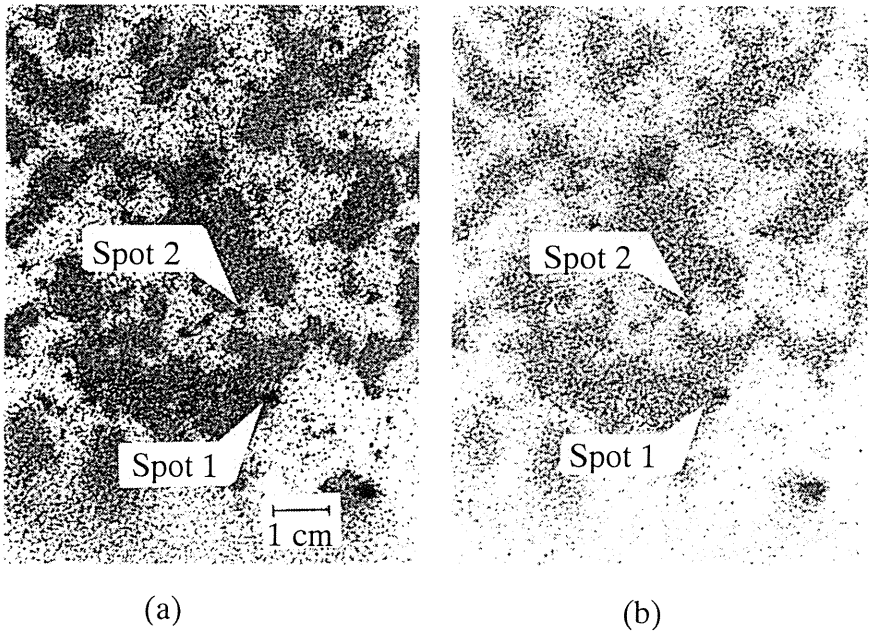

Fig. 4-4 IP images of a granite surface obtained by multilayer lamination exposure for 73 h. (a) The first layer image; spot 1 and 2 are rather strong radioactive spots. (b) The second layer image.

4.2.2 Images of natural radioactivity and radioactivity content

Figure 4-4(a) shows the IP image of the first layer of a two sheets lamination exposed to the surface of a piece of granite in the shielding box for 73 hours, and Fig. 4-4(b) shows the second layer image[4-8,4-9]. The radioactivity of spot 1 or 2 can be determined by comparing PSL intensities of standard samples with known radioactivity as described later. Figure 4-5 shows a photograph (a) of a cloisonne ware and its IP image (b) obtained by exposure for 93 h in the shielding box[4-10]. Some kinds of glaze paint contain radioactivity equivalent to ^{137}Cs β-rays of about 0.01 counts/mm^2· min. Although it is said that glaze paints generally contain uranium series, this cloisonne ware has thin glass glaze on the surface; alpha particles therefore cannot contribute to making the image.

Figure 4-6 shows the images of radioactivity of lotus root, sweet potato, white potato, ginger and pumpkins obtained by exposing for 20 days in the graded shielding box. Seeds in pumpkin and skin part in potato contain more radioactivity than other parts. Figure 4-7 shows the images of sea foods. Tang contains rather large amount of radioactivity, whereas shell does not. Since tang is thin, high energy β-rays, $E_{\beta\,max}$ = 1.46 MeV from ^{40}K, print the image with larger size than the real one and the shadow of a part of the shell can be seen.

Vegetables were ground to uniformly mix up and the γ-ray spectrum was measured with HPGe detector. Any other new γ-rays except for ^{40}K γ-rays couldn't be observed in the γ-ray spectra. KCl solution (^{40}K abundance in natural K is 0.0119%) with known content was also measured and the γ-ray intensity was compared with vegetable one. ^{40}K contents are given to be between 0.07 ~ 0.4 Bq/g depending on materials. ^{40}K β-rays, β-decay branching ratio of 89.3%, mainly contribute to make images. Radioactivity distribution images of vegetables, sea foods, meat and antique arts will give new information in the field of botany, oceanography, biology and archeology.

4.3 Identification of radionuclide species

It is generally wanted to know the radionuclide species and it is necessary to know the nuclide when we want to determine the radioactivity (Bq), because the average PSL intensity of a single radiation incidence is different for different radiations. It is possible to estimate the nuclide by referring to an absorption curve obtained by insertion of absorbers having different thickness between the specimen and the IP and by exposing several times repeatedly, which needs several days exposure. So, we tried the following two methods which needed only a single exposure.

(1) Several sheets lamination method

Figure 4-8 shows the relative intensity of five sheets of IP which were laminated in layers and exposed simultaneously to various radioactive reference sources with known radioactivities. The effect of γ-rays for ^{60}Co, ^{137}Cs and ^{241}Am can be seen. Since β-rays from ^{14}C and ^{147}Pm cannot penetrate even a single layer, nuclides emitting low-energy β-particles cannot be distinguished from each other.

(2) Several times successive read-out method

The latent image is read by scanning the IP with a laser beam and then the IP is usually erased by lightening for re-use. We read a single IP successively several times. Figure 4-9 shows the relative (PSL) intensity which depends on the kind of radiation and β-ray energy.

For spots 1 and 2 in the first sheet of Fig. 4-4, the results of multiple successive readouts are shown in Fig. 4-9 together with those for standard sources. The dotted lines, which may be seen as if they are connecting the experimental points, were obtained by the following semi-experimental equations:

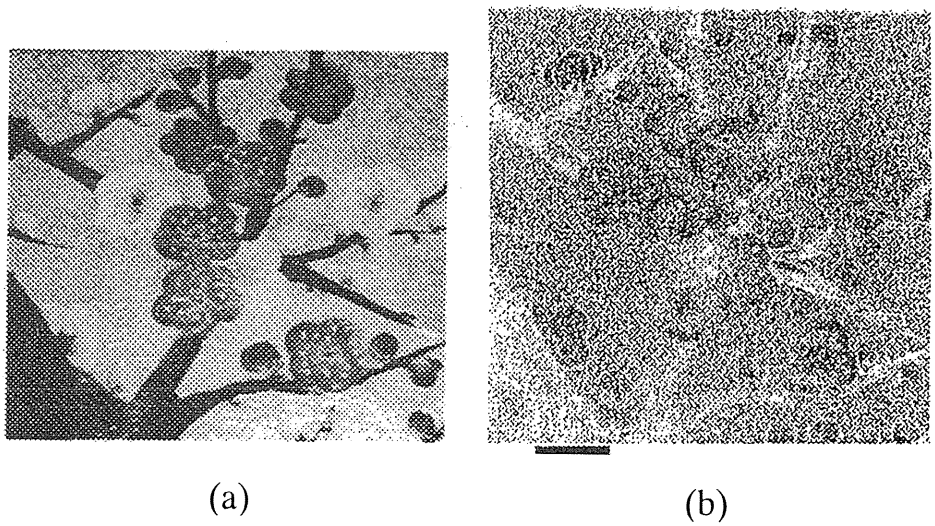

Fig. 4-5 (a) Real photograph of cloisonne ware, a figure of plum tree twigs with blossoms, and (b) its IP image obtained by 93 h exposure.

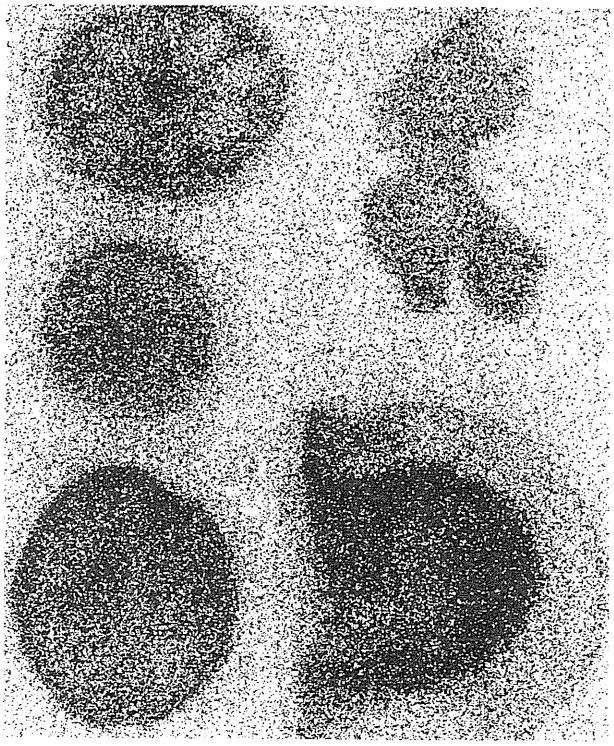

Fig. 4-6 Natural radioactivity distribution images of lotus root, sweet potato, while potato, ginger and pumpkin.

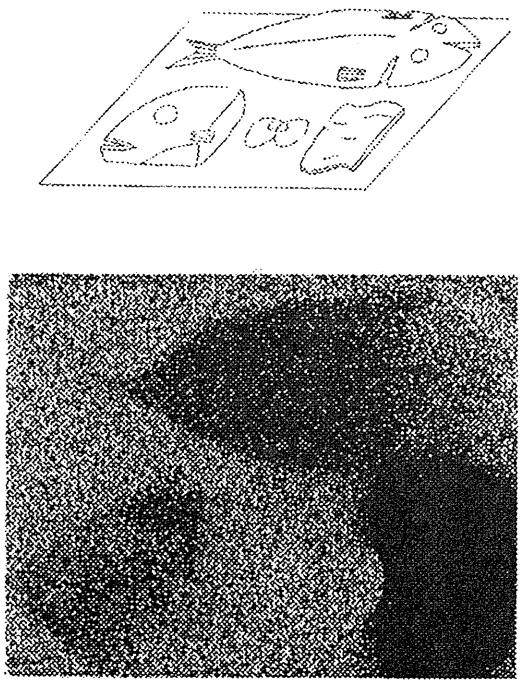

Fig. 4-7 Natural radioactivity distribution images of sea foods.

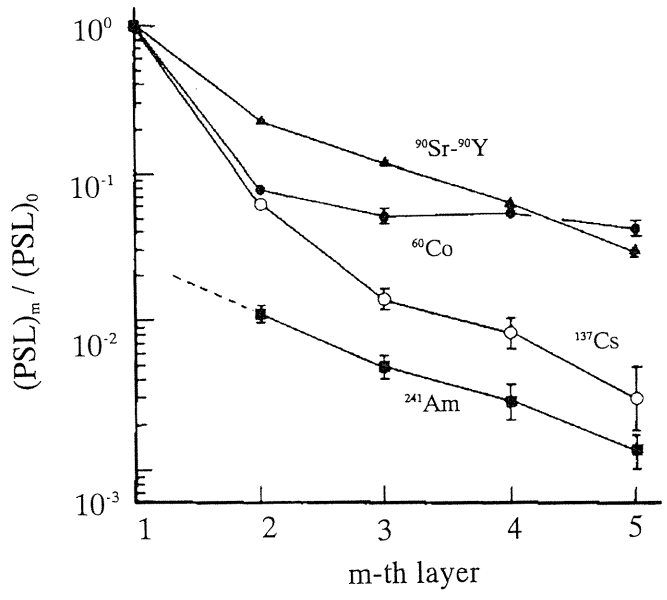

Fig. 4-8 Several sheets lamination method; relative PSL intensity at each layer, exposed to various radioactive sources.

$$F(m) = \frac{L_m}{L_1}$$

$$= (k_{m-2})^2\left\{1 - an_e k_{m-2}\left(1 - \frac{b}{(m-1)^2}\right)\right\}^2$$

$$\times \left(1 - \frac{b}{m^2}\right)/(1-b)\,,$$

$$k_0 = 1\,,$$

$$k_m = k_{m-1}\{1 - an_e k_{m-1}(1 - b/m^2)\}\,, \qquad (4\text{-}3)$$

where m means m-th in the readout times, L_m is the PSL intensity in the m-th reading, and a_{ne} and b are constants depending on the radiation kind and energy. Spot 1 in Fig. 4-4 shows a similar tendency as the ^{137}Cs curve. Then the intensity of radiation was determined to be 1.73 counts/min, equivalent to ^{137}Cs beta-particles by comparing with the PSL intensity of a ^{137}Cs standard source. On the other hand, spot 2 shows a tendency to similar ^{147}Pm. If spot 2 is a soft beta emitter like ^{147}Pm, it must not make any spot on the second sheet. On the second sheet, however, there appeared spot 2. We can therefore deduce that spot 2 contains two different nuclides; one is a $\beta(\gamma)$ emitting nuclide almost equivalent to ^{137}Cs, taking into

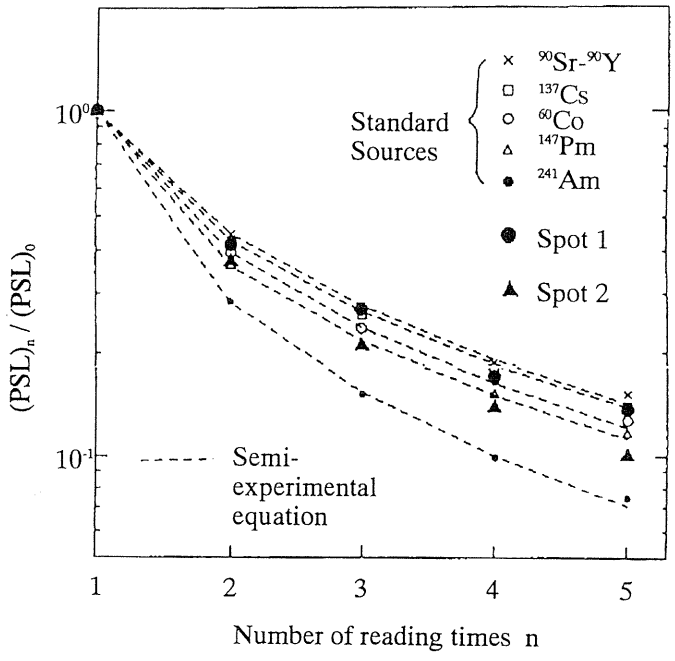

Fig. 4-9 Several times reading of successive readout method and application to the spot 1 (large spot) and the second spot (large triangles) in Fig. 4-4 together with several standard radioactive sources (small dots, etc.). Broken lines were obtained by Eq. 4-3 for standard sources.

account the result of spot 1, and the other is an alpha emitting nuclides. For spot 2 the following equation was applied.

$$F(m) = \frac{\{AF_{\alpha}(m) + BF_{\beta}(m)\}}{(A+B)} \tag{4-4}$$

where, A is the proportion of alpha emitting nuclides and B is that of beta emitting nuclides. The curve calculated with A = 0.48 and B = 0.52 fit well with the experimental result shown in Fig. 4-9, which gave 0.17 counts/min equivalent to alpha particles and 0.43 counts/min equivalent to ^{137}Cs beta radiations. The unit counts/min or counts/mm^2 · min should more precisely be expressed as (number of interactions)/min or so. The number of interactions of the radiation including γ-rays is almost the same as the number of counts detected with a 2π proportional counter which was used for the determination of radiation intensity of standard sources. It will be possible to convert N counts/min to an apparent radioactivity 2N/60 Bq. The error included in N counts/min is roughly estimated to be ± 30%.

V. Conclusions

Some new and unique position-sensitive proportional counters (PSPC) were developed and they found new applications. A single resistive anode wire PSPC was applied to the absolute radioactivity measurement of gaseous samples, which was adopted in Japan Atomic Energy Research Institute, et al. Slender and long neutron PSPC's were developed as ^{3}He counter, and nuclear fission counter, and they were used for the real-time measurements of neutron flux distributions in Kyoto University Critical Assembly (KUCA).

Optical fiber position detection method was newly developed. The tip of a fiber was painted with a mixture of ZnS(Ag) scintillator, neutron converter and adhesive material. The fiber was moved under a computer control. The detector was able to insert in very narrow space with 2 ~ 3 mm gap. By changing neutron converter, thermal neutrons, fast neutrons and even γ-ray distributions were measured. The method is now adopted in KUCA and in Phoenix Memorial Reactor in The University of Michigan.

The characteristics of Imaging Plate were examined and some new phenomena were found. Geometrical distributions of natural radioactivity contained in vegetables, meat, rocks, etc. were observed under the reduced natural radiation background with a heavy shielding box.

Acknowledgments

The research works mentioned in this report were heavily indebted to the staff members and the students of our laboratory. The author would like to express his sincere thanks to them and also to the relevant persons in our Department of Nuclear Engineering and other research institutes.

References

2-1) H.S. Carslaw and J.C. Jaeger "Conduction of Heat in Solids" (Oxford, 1956) p.92.
2-2) C. Mori, T. Aoyama and T. Watanabe, J. Nucl. Sci. Technol., **23**, 214 (1996).
2-3) M. Matoba, M. Tsuji, K. Marubayashi and T. Shintake, Nucl. Instr. Meth., **165**, 469 (1979).
2-4) C. Mori and T. Watanabe, J. Nucl. Sci. Technol., **22**, 461 (1985).
2-5) C. Mori, Y. Fujii and T. Watanabe, Appl. Radiat. Isotopes, **A38**, 371 (1987).
2-6) C. Mori, Y. Fujii and T. Watanabe, Appl. Radiat. Isotopes, **A38**, 379 (1987).
2-7) W.M. Augustyniak, W.L. Brown and H.P. Lie, IEEE Trans. Nucl. Sci., **NS-19**, 106 (1972).
2-8) S. Kalbitzer and W. Melzer, Nucl. Instr. Meth., **56**, 301 (1967).
2-9) A. Uritani, C. Mori, T. Watanabe and A. Miyahara, J. Nucl. Sci. Technol., **26**, 1094 (1989).
2-10) M.K. Copp, K.H. Valentine, L.G. Christophorou and J.G. Carter, Nucl. Instr. Meth., **201**, 395 (1982).
2-11) Y. Takenaka, A. Uritani and C. Mori, Houshasen [in Japanese], **19**[2], 33 (1993).
2-12) Y. Takenaka, A. Uritani and C. Mori, J. Nucl. Sci. Technol., **32**[4], 295 (1996).
2-13) R.B. Owen, M.L. Awcoch, IEEE Trans. Nucl. Sci., **NS-15**, 290 (1968).
2-14) P.W. Nicholson, "Nuclear Electronics", (John Wiley & Sons, Norwich, 1974) p.146.
2-15) T. Agui, H. Nagahashi and H. Takahashi, "Neural Program" [in Japanese] (Shoukou-dou, Tokyo, 1993) pp.11–20.
2-16) A. Uritani, C. Mori, T. Watanabe and A. Miyahara, Nucl. Instr. Meth., **A299**, 231 (1990).
2-17) A. Uritani, "Development and Application of New Type Position-sensitive He-3 Proportional Counter," Ph.D. Thesis, Nagoya University (1992).
2-18) W.B. Mann, H.H. Seliger, W.E. Marlow and R.W. Medilock, Rev. Sci. Instr., **31**, 690 (1960).
2-19) C. Mori, M. Nakamoto, A. Uritani and T. Watanabe, J. Nucl. Sci. Technol., **21**, 942 (1984).
2-20) C. Mori, A. Uritani and T. Watanabe, J. Nucl. Sci & Technol., **25**, 341 (1988).
2-21) C. Mori, T. Aratani, T. Watanabe and M. Yoshida, Appl. Radiat. Isotopes, **33**, 851 (1987).
2-22) M. Yoshida, Y. Wu, Y. Ohi, T. Senda, Radioisotopes [in Japanese], **42**[8], 452 (1993).
2-23) Y. Wu, C. Mori, T. Yamamoto, K. Yanagida, H. Miyahara, T. Aoyama and M. Yoshida, Radioisotopes, **42**[4], 209 (1993).
2-24) M. Yoshida, T. Yamamoto, Y. Wu, T. Aratani, A. Uritani and C. Mori, Nucl. Instr. Meth., **A330**, 158 (1993).
2-25) Y. Wu, C. Mori, A. Uritani, K. Yanagida, H. Miyahara, T. Aoyama and M. Yoshida, Nucl. Instr. Meth., **A343**, 539 (1994).
2-26) K. Kobayashi, J. Horie, K. Kanda, T. Shibata, Nucl. Sci. Eng., **71**, 143 (1979).
2-27) C. Mori, T. Haga and A. Uritani, Nucl. Instr. Meth., **A310**, 437 (1991).
2-28) C. Mori, A. Ando, A. Uritani and T. Haga, Houshasen [in Japanese], **21**[1], 35 (1995).
2-29) A. Uritani, C. Mori, T. Watanabe and A. Miyahara, J. Nucl. Sci. Technol., **27**, 712 (1990).
2-30) S. Kahn, R. Harman and V. Forgue, Nucl. Sci. Eng., **23**, 8 (1965).
2-31) A.O. Hanson and J.L. McKibben, Phys. Rev., **72**, 673 (1947).
2-32) L.V. East, R.B. Walton, Nucl. Instr. Meth., **72**, 161 (1969).
2-33) H. Toyokawa, A. Uritani, C. Mori, N. Takeda and K. Kudo, Proceedings of 8th ASTM-EURATOM Symposium on Reactor Dosimetry, 1993, Vail, Colorado.
2-34) K. Kudo, A. Fukuda, Y. Kawada, N. Kobayashi and N. Hayashi, Bulletin of Electrotechnical Laboratory, **54**, 248 (1990).
2-35) R.E. Textor and V.V. Verbinski, ORNL 4160 (1968).
2-36) JENDL-3 Compilation Group, Japanese Nuclear Data Committee: Japanese Evaluated Nuclear Data Library, Version-3-JENDL-3, JAERI 1319 (1990).
2-37) ICRP, "Data for Use in Protection Against External Radiation (ICRP Publication 51)," (Pergamon Press, Oxford, 1987) pp.74.
2-38) H. Toyokawa, A. Uritani, C. Mori, N. Takeda and K. Kudo, IEEE Trans. Nucl. Sci., **42**, 644 (1995).

2-39) W.N. McElroy, S. Berg. T. Crockett and R. Hawkins, AFWL-TR-67-41, vol.1, (Air Force Weapons Laboratory, Kirkland, 1967).
3-1) C. Mori, T. Osada, K. Yanagida, T. Aoyama, A. Uritani, H. Miyahara, Y. Yamane, K. Kobayashi, C. Ichihara and S. Shiroya, J. Nucl. Sci. Technol., **31**, 248. (1994).
3-2) C. Mori, K. Yanagida and T. Osada, Houshasen [in Japanese], **21**, 79 (1995).
3-3) C. Mori, Y. Mito, K. Yanagida, K. Kageyama, Y. Kuniya, A. Uritani, H. Miyahara, Y. Yamane, T. Misawa, K. Kobayashi, C. Ichihara, S. Shiroya, M. Hayashi, H. Unesaki, Proc. of 29th Academic Symposium at Kyoto Unv. Res. Reactor Inst. (1995 Feb., KURRI) p.193.
4-1) J. Miyahara, K. Takahashi, Y. Amemiya, N. Kamiya and Y. Sato, Nucl. Instr. Meth., **A246**, 572 (1986).
4-2) K. Takahashi, K. Kohda, J. Miyahara, Y. Kanemitsu, K. Amitani and S. Shionoya, J. Lumin., **31 & 32**, 572 (1984).
4-3) C. Mori and A. Matsumura, Nucl. Instr. Meth., **A312**, 39 (1992).
4-4) C. Mori A. Matsumura, T. Suzuki, H. Miyahara, T. Aoyama and K. Nishizawa, Nucl. Instr. Meth., **A339**, 278 (1994).
4-5) T. Suzuki, C. Mori, A. Matsumura and K. Yanagida, Housyasen [in Japanese], **21**[1], 43 (1995).
4-6) C. Mori, T. Suzuki, S. Koido, A. Uritani, H. Miyahara, K. Yanagida, J. Miyahara and K. Takahashi, Mucl. Instr. Meth., **A369**, 544 (1996).
4-7) C. Mori, T. Suzuki, S. Koido, A. Uritani, H. Miyahara, K. Yanagida, Y. Wu, K. Nishizawa, M. Yoshida, F. Takahashi and J. Miyahara, J. Radioanaly. Nucl. Chem., Articles, **206**[2], 263 (1996).
4-8) C. Mori, T. Suzuki, S. Koido, H. Miyahara, A. Uritani, T. Aoyama and K. Nishizawa, Nucl. Instr. Meth., **A353**, 371 (1994).
4-9) C. Mori, Housyasen [in Japanese], **20**[3], 13 (1994).
4-10) C. Mori, S. Koido, T. Suzuki, J. Miyahara and K. Takahashi, Radioisotopes [in Japanese], **44**[7], 3 (1995).